View metadata, citation and similar papers at core.ac.uk

brought to you by CORE

provided by Cronfa at Swansea University

A Hybrid Calibration Approach to Hertz-Type Contact Parameters for Discrete Element Models

Tongming Qu[a], Y.T. Feng[a], T. Zhao[a], Min Wang[b]

[a]Zienkiewicz Centre for Computational Engineering, College of Engineering, Swansea University, Swansea, Wales SA1 8EP, UK [b]T-3 Fluid Dynamics and Solid Mechanics Group, Theoretical Division, Los Alamos National Laboratory, Los Alamos, New Mexico, 87545, USA

Abstract

This study aims at providing a hybrid calibration framework to estimate Hertz-type contact parameters (particle-scale shear modulus and Poisson's ratio) for both two-dimensional and three-dimensional discrete element modelling. Based on statistically isotropic granular packings, a set of analytical formulae between macroscopic material parameters (Young's modulus and Poisson's ratio) and particle-scale Hertz-type contact parameters for granular systems are derived under small-strain isotropic stress conditions. However, the derived analytical solutions are only estimated values for general models. By viewing each DEM modelling as an implicit mathematical function taking the particle-level parameters as independent variables, and employing the derived analytical solutions as the initial input parameters, an automatic iterative scheme is proposed to obtain the calibrated parameters with higher accuracies. Considering highly non-linear features and discontinuities of the macromicro relationship in Hertz-based discrete element models, the adaptive moment estimation algorithm is adopted in this study due to its capacity of dealing with noise gradients of cost functions. The proposed method is validated with several numerical cases including randomly distributed monodisperse and polydisperse packings. Noticeable improvements in terms of calibration efficiency and accuracy have been made.

Keywords: Discrete element method; Hertz-Mindilin contact model, Calibration; Constitutive law; Adaptive moment estimation, Non-linear elastic model.

Nomenclature

k_n	normal contact stiffness
k_s	tangential contact stiffness
δ_n	normal contact displacement, $\delta_n = (R_1 + -R_2 z)$
R_1	the radius of particle 1
R_2	the radius of particle 2
r	the radius of monodisperse particles
z	the distance between the centers of two particles
_	the effective radius of the contact

R

f_n the normal contact force between two particles

s_{ijc} the interparticle contact flexibility tensor at the c^{th} contact

u^c the contact overlap at the c^{th} contact

Δf_i^c the force increment at the c^{th} contact

G^* particle-scale shear modulus

E^* particle-scale Young's modulus

v^* particle-scale Poisson's ratio

$\boldsymbol{n}^c$, $\boldsymbol{s}^c$ and $\boldsymbol{t}^c$ three vectors of the local coordinates constructed at the c^{th} contact

θ the polar angle in the polar coordinate system

γ, β the polar angle, and azimuthal angle in a spherical coordinate system

L_{cj} the *branch vector* connecting centroids of particles in c^{th} contact

V the volume of a three-dimensional particle assembly

S the area of a two-dimensional particle assembly

N_c the total number of interparticle contacts in the volume V

A_{jk} a second-order tensor associated with the particle structure

n_{kc} the unit outward normal vector at the contact interface of contact c

δ_{ij} Kronecker tensor

S_{ijkl} compliance tensor

ε_{ij} strain tensor

σ_{kl} stess tensor

$\rho\theta(\ )$ contact density in two-dimensional models $\rho\gamma\beta(\ ,\ )$ contact density in three-dimensional models

σ_c istropical confining stress

E the equivalent Young's elastic modulus of a granular assembly

v the equivalent Poisson's ratio of a granular assembly

G the equivalent shear modulus of a granular assembly

$\bar{N}_c$ the average coordination number in a granular assembly

ϕ the porosity in a granular assembly

N_p the total number of particles

S_v the total area of the voids

V_v the total volume of the voids

S_p the total particle area in a granular assembly

V_p the total particle volume in a granular assembly

C_u uniformity coefficient

d_{50} median diameter

d_{40} the diameter below 40% of the total particles

d_{60} the diameter below 60% of the total particles

t iterative number

E_t the targeted Young's modulus of a granular assembly

ν_t the targeted Poisson's ratio of a granular assembly

M_t an exponentially decaying average of past gradients of the cost function

G_t an exponentially decaying average of past squared gradients of the cost function

g_t the gradient of the cost function at the t^{th} iterative step

λ_1, λ_2 weighting coefficients of the cost function

β_1 a decay rate of the first-moment of the gradient

β_2 a decay rate of the second-moment of the gradient

θ_i independent variables during the Adam iterative process

$\bar{G}$ initial particle scale shear modulus

$\bar{\nu}$ initial particle scale Poisson's ratio

$G^{\cdot}$ normalized particle-scale shear modulus

$\nu^{\cdot}$ normalized particle-scale Poisson's ratio

$\Delta G^{\cdot}$ small increments of the normalised particle-scale shear modulus $G^{\cdot}$

$\Delta \nu^{\cdot}$ small increments of the normalised particle-scale Poisson's ratio $\nu^{\cdot}$

α learning rate

$\boldsymbol{g_t}$ the gradient of the cost function

η a hyperparameter to determine the first increments of independent variables

1 Introduction

Many studies have confirmed the ability of discrete element modelling (DEM) to capture intrinsic features of granular materials (Bourrier, et al.[1], Sibille, et al.[2], Nicot, et al.[3], Wang, et al.[4], Wang, et al.[5], Liu, et al.[6], Qu, et al.[7], Wang, et al.[8], Cambou, et al.[9], Wautier, et al.[10], Dugelas, et al.[11], Qu, et al.[12], Gao and Meguid[13, 14]). However, the choices of DEM parameters are often made in a trial and error manner (Coetzee[15, 16], Qu, et al.[17]). A barrier to determining reasonable contact parameters is that a direct measure of particle-scale parameters is difficult to achieve for granular systems with several different constituents. Additionally, DEM models simplify the complexity of real physical systems, such as contact, particle geometry and particle deformation, and also often reduce the number of particles involved. Even if particle-scale parameters can be accurately measured, the measured data is not necessarily suitable for discrete element modelling. Thus the philosophy of calibration is admitting these numerical simplifications and tuning or calibrating the DEM model to capture the major responses observed in physical laboratory tests (O'Sullivan[18]).

The calibration of DEM parameters, by its nature, is an *inverse problem*, which determines the causal factors (particle-scale parameters) from some measures or observations (macroscopic responses). The corresponding *forward problem* is predicting the macroscopic stress-strain relations of a particle assembly based on particle-scale parameters. This forward problem receives great interests to material science and physics and is widely investigated based on homogenisation methods to link continuum-based mechanics to the non-continuum particle-scale characteristics (Satake[19], Bagi[20]).

In the past, various homogenisation methods are developed to derive micro-macro relationships of granular materials, such as *Voigt's hypothesis* (*kinematic assumption*) (Liao, et al.[21], Kruyt and Rothenburg[22], Chang and Lun[23], Digby[24], Walton[25], Chang, et al.[26]), *Reuss's hypothesis* (*static assumption*) (Chou, et al.[27], Li, et al.[28], Chang and Liao[29], Yimsiri and

Soga[30]), *best-fit hypothesis* (Liao, et al.[21], Liao, et al.[31]) and *Piece-wide fit hypothesis* (Liao, et al.[21]). Some recent works aimed at defining a relevant mesoscale to link continuum-based mechanics at the macroscopic scale (Zhu, et al.[32], Zhu, et al.[33], Zhu, et al.[34], Xiong, et al.[35]), precisely to circumvent the non-continuum microscopic characteristics at the contact scale.

Although various hypothesises are involved and sophisticated formulations have been derived, the accurate prediction of constitutive relations of granular materials remains to be an outstanding issue. The reason for failure to accurately predict constitutive relationships of granular materials may be attributed to the fact that most homogenisation methods are derived from the continuum-based theory (Goldenberg, et al.[36]). Granular systems are observed to transfer internal forces in a chain-like (discontinuous and inhomogeneous) way when subjected to external loads (Ouaguenouni and Roux[37], Sun, et al.[38], Pouragha, et al.[39], Nicot, et al.[40]). The existing literature has shown that the continuum elasticity is valid only under certain conditions for granular materials (Goldenberg and Goldhirsch[41],[42]). However, the current knowledge about force-transmission mechanisms in granular materials (such as force chains) is still incapable of connecting the micro elasticity to the macro elasticity.

Statistical or optimisation based algorithms become popular to determine particle-scale parameters in DEM as an inverse problem. Existing algorithms include the response surface methodology (Yoon[43]), artificial neural networks (Benvenuti, et al.[44], Zhou, et al.[45]), Latin hypercube sampling and Kriging (Rackl and Hanley[46]), random forest (Boikov, et al.[47]), the genetic algorithm (Pachón-Morales, et al.[48], Do, et al.[49]), the sequential quasi-Monte Carlo (Cheng, et al.[50]) and the Bayesian approach (Cheng, et al.[51]). Although these algorithms are useful to quantify a wide range of complex problems, their applications alone still suffer from numerical issues such as local optimum and time-consuming iterative process. Particularly, the development of statistical or optimisation based algorithms cannot replace the study on underlying physical laws.

As the continuation of a sequence of work to address parameter calibration problems in DEM, the main objective of this paper is to extend a hybrid analytical-computational framework proposed in (Qu, et al.[52]) to effectively approximate the contact parameters in the pressuredependent Hertz-Mindlin-type contact models for both 2D and 3D cases. Based on Reuss's hypothesis, a set of simplified static solutions relating particle-scale contact stiffnesses to macro material properties for Hertz-Mindlin-type contact models are explicitly derived in Section 3 and compared with the numerical results in Section 4. These semi-analytical formulae are then served as the initial estimation for the subsequent iterative scheme that aims to further improve the calibration accuracy numerically. However, due to the highly nonlinear feature of discrete particle systems which is made worse by the nonlinear relationship in the HertzMindlin-type contact model, the gradient-based iterative scheme adopted in (Qu, et al.[52]) tends to suffer from poor convergence for the problem concerned. Thus an alternative algorithm called the adaptive moment estimation (Adam) (Kingma and Ba[53]) that is developed for machine learning, is employed in Section 5 to automatically optimise the parameters to be calibrated. The detail of the algorithm and related computational aspects are provided and discussed. The numerical examples are also presented to demonstrate the performance of this hybrid calibration procedure for both monodisperse and polydisperse granular systems.

2 Hertz contact law and interparticle behaviour

The Hertz-Mindlin-type contact model remains the foundation for most contact problems encountered in engineering due to the relative rationality and simplicity. Under the condition that the surfaces of contacting elastic spheres are perfectly smooth, the relation between the normal contact force f_n and normal contact overlap δ_n can be given by:

$$f_n = \frac{2(2\sqrt{2})R^{*1/2}\bar{G}}{3(1-\nu^{*})}\delta_n^{3/2} \tag{1}$$

where G^* and v^* are the shear modulus and Poisson's ratio of the particles; the overlap $\delta_n = +-(R_1 \quad R_2 \quad z)$, with R_1 and R_2 being the radii of the two particles and z being the distance between the two particle centres; and $\bar{R}$ is the effective radius of the contact defined as

$$\bar{R} = \frac{2RR_{1\,2}}{R\,R_1 + {}_2}.$$

The normal contact stiffness k_n is derived as the derivative of the normal force to the normal displacement δ_n:

$$k_n = \frac{\partial f_n}{\partial \delta_n} = \frac{(2)\bar{R}\,G^{1/2\,*}}{(1-\nu)^{1/2}}\delta_n = \frac{3\bar{R}G^{*2}}{(1-\nu)^{1/3}}f_n \tag{2}$$

The shear force is dependent on the deformation at the contact and the history of sliding, and is therefore complicated in its formulation. Based on different simplifications, several different formulations for shear stiffnesses are reported in the literature (Yimsiri and Soga[30], Itasca[54], Chang, et al.[55], Cundall[56], Tsuji, et al.[57]). Different shear stiffness formulations do yield different macro-micro expressions as shown in Section 3, but their actual differences are rather limited. Considering the interests of our current work, these comparisons are not presented here. In this paper, a simple and commonly used formulation for the Hertz stiffness ratio (shear stiffness k_s to normal stiffness k_n) is adopted as (Cundall[56])

$$\frac{k_s}{k_n} = \frac{2(1-\nu^*)}{2-\nu_*} \tag{3}$$

Note that, although the Hertz contact model is developed for elastic spheres, we also apply it to 2D discs by treating the law as a nonlinear power-law, as a supplement of the linear elastic model. Thus, both 2D disc and 3D sphere cases are described below. It is also straightforward to implement other Hertz-type formulations for specific applications by following our proposed framework.

Let s_{ij}^c be the interparticle contact flexibility tensor at the c^{th} contact. The relationship between the contact overlap u_j^c (treated as a vector) and the contact force f_i^c at the contact is given by:

$$u_{cj} = s\, f_{ijc} \qquad ic \tag{4}$$

As Fig. 1 shows, let the contact vector **n** be the direction normal to the contact plane and the vectors **s** and **t** be the directions transversal to the contact plane. Assuming that the shear contact stiffnesses in the **s** and **t** directions are the same and no coupling effect occurs between the normal and shear directions. The contact flexibility tensor s_{ij}^c can be expressed in terms of the unit vector $\boldsymbol{n}^c$, $\boldsymbol{s}^c$ and $\boldsymbol{t}^c$ of the local coordinate system constructed at the c^{th} contact (Hicher and Chang[58]):

$$s_{ij}^c = \frac{1}{k_n} n_i^c n_j^c + \frac{1}{k_s}\left(s_i^c s_j^c + t_i^c t_j^c\right) \tag{5}$$

Considering the contact vectors $\boldsymbol{n}^c$, $\boldsymbol{s}^c$ and $\boldsymbol{t}^c$ in contact planes that are transverse isotropic, the flexibility tensor s_{ij}^c can be simplified as another expression as reported in (Zhu, et al.[59]):

$$s_{ij}^c = \frac{1}{k_n} n_i^c n_j^c + \frac{1}{k_s}\left(\delta_{ij} - n_i^c n_j^c\right) \tag{6}$$

where $\boldsymbol{n}^c$ can be expressed as follows (Hicher and Chang[60])(see Fig. 2 for the 2D coordinate system):

$$\boldsymbol{n}^c = (\cos\theta, \sin\theta) \qquad (2D) \tag{7}$$

$$\boldsymbol{n}^c = (\cos\gamma, \sin\gamma\cos\beta, \sin\gamma\sin\beta) \qquad (3D)$$

3 Semi-analytical solutions for predicting Hertz-type contact parameters

The stress-strain relationships for granular materials have received great attention in the past. Based on the static assumption, the relationships can be described with both particle-scale normal and tangential contact stiffnesses. A detailed derivation of the stress-strain relationships of randomly distributed monodisperse packing with Hertz-Mindlin-type contact models is provided in Appendix under the conditions: (1) small strain conditions; and (2) statistically isotropic packings. In this Section, formulae for estimating particle-scale parameters are given for general cases. A set of semi-analytical solutions for directly predicting Hertz-type contact parameters are also offered.

3.1 Analytical prediction of Hertz-type contact parameters

In DEM simulations, the particle shear modulus G^* or elastic modulus E^* and particle Poisson's ratio ν^* are the input parameters of the Hertz-type contact model. According to the Appendix, when the macro-material properties (Young's modulus E and Poisson'rato ν) of a statistically isotropic monodisperse granular packing are given, the corresponding particlescale parametersG^*, E^* and ν^* can be analytically obtained as:

2D case:

$$\nu^* = \frac{8\nu}{1+7\nu} \tag{8}$$

$$E_* = 3N5(1\ 15)_c + \nu_2 \square\square\ \overline{E_2}\square\square\ \square\square(1-\nu\sigma)_{\ c}\square\square_{-_12} \tag{9}$$

$$(1\ 7)+\nu\ \square r\ \square$$

$$G_* = 6\overline{SN_c}\square\square\square\ \overline{E_2}\square\square\ \square\overline{\square\square(1+7\nu)}\sigma_c\square\square\square \tag{10}$$

$$(1+7\nu)r$$

3D case:

$$\nu^* = \frac{10\nu}{8\nu+1} \tag{11}$$

$$E_* = 16V\ (18+1\nu_2)\ E_2\ _2\ \sigma\ \nu_c\ (1\ 2\ ) - \tag{12}$$

$$N_c\ (8+1\nu\ )\ r\ \ 6$$

$$G_* = V\ \ _2 E\ \ \ (1\ 2-\nu)\sigma_c \tag{13}$$

$$N_c\ 4\ (r\ 8\nu+1)\ \ 6(8\nu+1)$$

In the above formulae, N_c is the total number of interparticle contacts in the area S/volume V of the granular assembly; r is the particle radius; σ_c is the confining stress applied.

3.2 Semi-empirical and semi-analytical solution for predicting Hertz-type contact parameters

The ratio of S/N_c (2D) or V/N_c (3D) governs the density of the granular packing and its value is not available unless the packing reaches a stable equilibrium state. From the perspective of physics, the density of a granular packing is associated with the particle shape and size distribution used, the confining stress applied, and how the packing is initially generated.

In this study, the coordination number $\bar{N}_c$ and the porosity ϕ are defined by:

$$\bar{N}_c = \frac{2N_c}{N_p} \tag{14}$$

$$\varphi = \begin{cases} S \\ \bar{S}_v \ \text{(2D)} \\ \hline \\ V_v \ \text{(3D)} \\ V \end{cases} \tag{15}$$

where N_p is the total number of particles, and S_v or V_v is the total area/volume of the voids. Assuming that the total area/volume of particles is S_p or V_p, then $V=V_v+V_p$ or $S=S_v+S_p$. For a monodisperse granular packing, the total particle area/volume can be determined by:

$$\begin{cases} S_p = N \pi r_p^2 & \text{(2D)} \\ V_p = N \frac{4}{3} \pi r^3 & \text{(3D)} \end{cases} \tag{16}$$

Combining Eqs. (14)-(16), the ratio of S/N_c (2D) or V/N_c (3D) is given by:

$$\begin{cases} \frac{S}{N_c} = \frac{2\pi r^2}{(1-\phi)N_c} & \text{(2D)} \\ \frac{V}{N_c} = \frac{8\pi r^3}{3(1-\phi)N_c} & \text{(3D)} \end{cases} \tag{17}$$

For a randomly distributed granular assembly, although the relationship between the porosity ϕ and the coordination number $\bar{N}_c$ is not unique, a proportional relationship has been proven to exist (Liao, et al.[31] , Hicher and Chang[60]). The coordination numbers and the porosities of some DEM packings are presented in Fig. 3. which shows that an approximately linear relationship can be found between the coordination number and the porosity.

In DEM models, the porosity of a granular assembly is highly influenced by the *initial friction coefficient* of particles used while generating the assembly. In this study, the initial coefficient of friction is used to control the porosity in a granular assembly. The relations between the initial friction coefficient and porosity of the specimens are shown in Fig. 4, indicating that the porosity in a specimen increases with the initial coefficient of friction. Note that the porosity here does not account for the overlap of contacts and is thus slightly lower than the experimental porosity.

Then the relation between the packing related parameter $(1-\varphi)\bar{N}_c$ and the numerical initial friction coefficient is investigated in both 2D and 3D DEM models with a large range of porosities. Fig. 5 shows that a quadratic relation is found for both 2D and 3D cases. The relevant fitted relation can provide a satisfactory estimation for the packing parameter $(1-\varphi)\bar{N}_c$ in randomly distributed granular packings. The actual porosity in a granular packing may slightly vary with the changes in the particle size distribution, particle numbers involved in models, and confining stress conditions, and thus the empirical formulae in Fig. 5 is simply an initial estimation. By combining Eqs. (17), (8)-(10), and (11)-(13), a set of initial estimation for particle-scale parameters can be given.

In the case that the estimation made by the provided empirical relations is found to be unsatisfactory during the subsequent iterative computations, a remedial measure that the S/N_c (2D) or V/N_c (3D) in the already generated model is used as a new approximation can be taken. The approximation will be further improved by the iterative scheme to be introduced in Section 5.

4 Comparisons between derived formulae and numerical tests

Several benchmark tests are performed to show the difference between the derived formulae and numerical tests. The comparisons offer more understanding of the derived formulae in Section 3. On the other hand, it also provides justifications for extending the derived formulae to polydisperse granular packings (see Section 4.3).

4.1 Benchmark test schemes

To numerically determine the equivalent elastic properties of a granular assembly, biaxial/triaxial tests with constant lateral confining pressure are performed using DEM (shown in Fig. 6).

In the presence of a constant confining stress, the equivalent elastic modulus and Poisson's ratio of granular materials can be numerically obtained as:

$$E=\left(\frac{\Delta\sigma}{\Delta\varepsilon}\right)_c \tag{18}$$

$$\nu=-\left(\frac{\Delta\varepsilon^L}{\Delta\varepsilon_T}\right)_c \tag{19}$$

where the subscript index c represents a constant confining stress condition; ε_L and ε_T are the strains in the loading and transverse directions, respectively.

4.2 Monodisperse granular packings

Several monodisperse granular assemblies enclosed in a square/cubic box are generated to evaluate the derived analytical solutions. The granular assemblies are isotropically compacted to a predefined stress state.

To prevent possible rearrangements of particles (irreversible plastic deformation) for the granular system subjected to a small strain condition, the initial coefficient of friction is then replaced with a relatively larger coefficient of friction (e.g. 1.0), prior to performing loading and unloading tests.

The model parameters used are listed in Table 1. Note that these parameters are rather arbitrally chosen to show the differences between the static analytical solutions and the DEM results.

A loading-unloading case can be used to check whether the granular specimen is in a state of elastic deformation during loading/unloading. The specimen is loaded along the vertical direction until the axial strain is up to a relatively small value (5×10^{-4} is adopted in our model). The axial deviatoric stress versus the axial strain is shown in Fig. 7. Although the Hertz-type contact model is non-linear, the small-strain Young's modulus still shows a response similar to

linear behaviour. Particularly, the unloading stress-strain curves perfectly match with the loading stress-strain curves, indicating that the granular specimen subjected to an axial strain of 5×10^{-4} is under an elastic state. This check is always recommended for a specific model due to two reasons: (1) the specimen before testing may not be in a sufficiently converged state (may affect the initial stress-strain curves); (2) the model porosities affect the range of the elastic region. i.e, the elastic region for a loose model may stop at a relatively small axial strain while the counterpart for a dense model exists even under a relatively large axial strain.

Figure 8 shows the comparison of Young's modulus between the DEM simulations and the static analytical solutions, with the initial friction coefficient ranging from 0 to 1. The results show that there are evident discrepancies between the DEM simulations and the static solutions. One of the main reasons responsible for the differences is that the static homogenisation hypothesis cannot incorporate the force-transmission features in granular materials, where external loads are transferred in a way totally different from that in continuum media (Luding[61], Peters, et al.[62], Zhang, et al.[63]).

The derived Poisson's ratio is analytically determined by the ratio of the normal stiffness to the tangential stiffness and is thus independent of confining stress, porosity and fabric. Figure 9 gives a comparison of Poisson's ratio between the analytical solution and the numerical solution. The difference between them increases as the porosity increases. A significant discrepancy between the analytical solution and the DEM simulations can be found. Similar results are reported in (Gaspar[64], Gu and Yang[65]). Gaspar (Gaspar[64]) reported that the reasons for the discrepancy of Poisson's ratio are attributed to the presence of a significant amount of heterogeneity caused by the heterodisperse nature of the simulation. Gu and Yang (Gu and Yang[65]) thought that the reason may be attributed to the fact that the stress exponent *n* for elastic modulus is higher than 1/3 as predicted by the Hertz-Mindlin law. Apart from these reasons,

the simplification of the tangential stiffness formulation may also give rise to some relative error between the analytical solution and DEM modelling.

Although the static analytical solutions alone cannot predict Young's modulus and Poisson's ratio with high accuracy, they do provide approximates which are relatively close to the true values, compared to an arbitrary guess. These approximate values will be effectively employed as the initial inputs in the next section to obtain the refined estimations.

4.3 Polydisperse granular packing

Although the analytical expressions (8)-(13) are derived based on the premise that the particles are equal-sized, they are extended here for polydisperse packings with the particle diameter $2r$ being replaced by the median diameter (d_{50}) of the polydisperse granular packing.

To find out how much error may be introduced by such an extension, 19 tests are conducted with various uniformity coefficients (C_u) but a fixed d_{50}:

$$C_u = d_{60}/d_{40} \tag{20}$$

where d_{60} and d_{40} are the diameters below 60% and 40% of the total particles, respectively. The particle size distributions employed for the simulations are shown in Table 2. Except for the first specimen, the radii of particles in the other specimens are evenly distributed between the minimum and maximum radii.

Figure 10 shows the differences between the DEM simulations and the static analytical solutions when the coefficient of uniformity (C_u) in a granular packing increases gradually. The derived Young's modulus decreases with an increase in the coefficient of uniformity in both 2D and 3D cases, which compensates the errors originally arising from the static hypothesis to a certain extent. Therefore, although the formulae (8) and (13) are derived from the monodisperse packing, both formulae will be employed as the initial guesses in the next section to obtain the refined estimations

5 Improved estimation scheme with a machine learning algorithm

5.1 The basic idea and framework for optimal estimation of particle-scale parameters

The key idea of our iterative methodology is to view the DEM simulation as an implicitly defining mathematical function (say: f), which takes the inputted Hertz-type parameters as independent variables (elastic modulus E^* and Poisson's ratio v^*) while the simulated macroscopic responses as the function value (say f_{dem}). Then an iterative scheme is used to solve an equation:

$$f_{\text{dem}}(E^*,v^*) = f_{\text{experiment}}, \text{ or } f_{\text{dem}}(E^*, v^*)\text{-}f_{\text{experiment}} = 0 \tag{21}$$

Then the calibration problem is converted to a problem of numerically finding roots of the implicitly defined mathematical equation. Nevertheless, this requirement is too strict, and it is almost impossible in this way to obtain the values of the parameters to be calibrated for general cases. Thus, the calibration problem has to be converted to a minimisation problem where the values of the parameters are sought to minimise the difference between the simulated macroscopic responses and the targeted values. There are in theory many numerical schemes available that could be employed to solve the minimisation problem, such as the Newton Raphson Method, and gradient-based methods (Qu, et al.[52], Madsen[66]).

However, for a highly nonlinear discrete granular system, particularly for the Hertz-type based DEM models, the traditional methods suffer from the problems of existing many local optimums and/or poor convergence. The gradient-based method proposed in our previous work (Qu, et al.[52]) for the calibration of linear contact parameters has proved to be inefficient and no successful calibration has been achieved for the current problem concerned.

The alternative optimisation method to be adopted in this study is the so-called adaptive moment method (Adam). This method was developed in 2015 in the field of machine learning

(Kingma and Ba[53]), and is appropriate for problems with very noisy gradients which is exactly the problem that a DEM model has. Our numerical tests to be presented in the section indicate that this method is superior to many traditional optimisation methods.

5.1.1 Cost function

As stated, the calibration procedure of particle-scale parameters for a granular assembly is equivalent to finding the values of the calibration parameters to minimise the difference between the targeted macroscopic properties and the actual values achieved numerically. The *cost* or *error function* to be minimised is constructed as:

$$L\,E(\,,\nu\,\lambda) = {}_{1}(\not{E}\,E_t - 1) + {}^{2}\lambda\nu\not{\nu}_2({}_t - 1)^2 \tag{22}$$

where E and ν are the equivalent Young's modulus and Poisson's ratio of the granular assembly; E_t and ν_t are the targeted Young's modulus and Poisson's ratio, respectively; λ_1 and λ_2 are two positive weighting coefficients with $\lambda_1 + \lambda_2 = 1$. When only Young's modulus is calibrated, λ_1=1 and $\lambda_2 = 0$. When both modulus and Poisson's ratio are calibrated with equal importance, λ_1=λ_2=0.5.

5.1.2 Optimisation with adaptive moment estimation (Adam)

As the equivalent Young's modulus E and Poisson's ratio ν are functions of the particle-scale shear modulus G^* and Poisson's ratio ν^*, the calibration procedure is now reduced to a minimisation problem with both G^* and ν^* being the variables to be sought. Considering the highly non-linear and discontinuous features of the cost function, a recently popular machine learning algorithm, the Adaptive Moment Estimation method (Adam) (Kingma and Ba[53], Ruder[67]), is adopted to optimise the calibration parameters. Adam is a first-order gradientbased optimisation of the cost function based on adaptive estimates of lower-order moments of a

gradient. The method is computationally efficient and works well on problems with noise gradients. Thus it is particularly suitable for the current problem.

The implementation of the Adam method requires computing an exponentially decaying average of past gradients (say M_t) and an exponentially decaying average of past squared gradients (say G_t) as follows:

$$M_t = \beta_1 M_{t-1} + -(1 \beta_1) g_t \tag{23}$$

$$G_t = \beta_2 G_{t-1} + -(1 \beta_2) g_t \otimes g_t \tag{24}$$

where the subscript t denotes the iterative number (starting from 1); g_t denotes the gradient of the cost function at the t^{th} iterative step; the symbol $\otimes$ represents element-wise multiplication; β_1 and β_2 are the decay rates of the first-moment and the second-moment of the gradient; and their values are typically initialised to 0.9 and 0.999, respectively.

Due to the fact that these moving averages are initialised as vectors of 0's, the moment estimates are biased towards zero at the initial timesteps and especially when both decay rates are close to 1 (Kingma and Ba[53]). This initialisation bias is practically corrected with biascorrected moment estimates as follows:

$$\hat{M}_t = \frac{M_t}{1-\beta_1^t} \tag{25}$$

$$\hat{G}_t = \frac{G_t}{1-\beta_2^t} \tag{26}$$

To find the minimum of a function using the Adam algorithm, independent variables (say θ_i) are iteratively updated by:

$$\theta_i := \theta_i - \frac{\alpha}{\sqrt{\hat{G}_t + \varepsilon}} \hat{M}_t \tag{27}$$

where α is the learning rate; the symbol ":= " means *assignment*; the symbol ε is a smoothing term usually initialised to a tiny number such as 10^{-8}.

The selection of the learning rate is not unique and the optimal value cannot be explicitly determined. Empirically, the learning rate can be chosen from 0.1, 0.01, and 0.001, depending on its influence on the optimisation process. The learning rate will affect the overall performance in terms of computational time and accuracy.

5.1.3 Feature scaling

Feature scaling is used to normalise the range of independent variables. Due to the fact that the raw data comes from different measures and has different scales, the gradient-based machine learning algorithm usually requires feature scaling to facilitate a faster converge of the iterative process. In our study, both particle-scale Young's modulus E^* and Poisson's ratio ν^*, are normalised by the initial values (denoted as E and ν, and given by Eqs. (8-9) or (11-13), and the resulting normalised Young's modulus $E^{\cdot}$ and Poisson's ratio $\nu^{\cdot}$ are expressed as:

$$E^{\cdot} = \frac{E^*}{E}, \quad \nu^{\cdot} = \frac{\nu^*}{\nu} \tag{28}$$

Now the cost function can be rewritten as:

$$L\,E(\,,\nu) = F\,E(\,^*,\nu^*) = f\,E(\,^{\cdot},\nu^{\cdot}) \tag{29}$$

5.1.4 Gradient approximation

Direct calculation of gradients is possible only when the closed-form expression of the cost function is already known. In contrast, the derived analytical solution in Section 3 is simply an estimation and the actual relationship between macroscopic parameters and particle-scale parameters is nearly impossible to determine. In this study, the finite-difference method is used to approximate the gradient (Feng, et al.[68]), i.e., let the gradient of the cost function $\boldsymbol{g_t}$ be:

$$\boldsymbol{g}_t = \left(\frac{\partial F}{\partial E^*}, \frac{\partial F}{\partial \nu^*}\right) \tag{30}$$

where the partial derivatives of the cost function are given as:

$$\begin{aligned} \frac{\partial F}{\partial E^*} &\approx \frac{\Delta F}{\Delta E} = \frac{f(E^* + \Delta E^*, \nu^*) - f(E^*, \nu^*)}{\Delta E^*} \\ \frac{\partial F}{\partial \nu^*} &\approx \frac{\Delta F}{\Delta \nu} = \frac{f(E^*, \nu^* + \Delta \nu^*) - f(E^*, \nu^*)}{\Delta \nu^*} \end{aligned} \tag{31}$$

where ΔE^* and $\Delta \nu^*$ are two (small) increments of the normalised particle-scale Young's modulus E^* and Poisson's ratio ν^*.

At the first iteration, ΔE^* and $\Delta \nu^*$ are set to be $\Delta E^* = \eta E^*$ and $\Delta \nu = \eta \nu^*$ where the parameter η is typically taken around ~0.1. For other iterations, ΔE^* and $\Delta \nu^*$ are taken to be the step increments of E^* and ν^* (refer to Eq. (27)). This means that the gradient of the cost function is approximated by its secant slope. With the purpose of constructing the partial gradients $\boldsymbol{g}_t$, the particle scale modulus and Poisson's ratio are updated three times in each iteration. The three updates correspond to $f(E^*, \nu^*)$, $f(E^* + \Delta E^*, \nu^*)$, $f(E^*, \nu^* + \Delta \nu^*)$, respectively, in Eq. (31).

When these parameters are changed, a new specimen is created and a re-equilibration is required. Except for the minor changes of the updated particle modulus and Poisson's ratio, the other input parameters or initial conditions such as the confining stress and the initial particle friction keep the same. Therefore, the void ratio and internal force-chains distributions are similar but not identical to the other specimens. The small variations in the granular fabric are also one of the sources of highly non-linear relationships between micro and macro parameters.

5.2 Numerical tests of the proposed with the proposed calibration framework

Four numerical cases including monodisperse random packings (Case 1 for 2D and Case 2 for 3D) and polydisperse random packings (Case 3 for 2D and Case 4 for 3D), are performed to show the robustness of the proposed method. The targeted Young's modulus and Poisson's ratio are 10GPa and 0.2, respectively, for all the test cases (assuming that they are experimentally determined material properties). Furthermore, the iterative process is terminated when the cost function is reduced to less than 10^{-4} or when no improvement is possible. All the numerical cases in this study are performed with Particle Flow Code (PFC) software. These DEM specimens are also made to a quasi-isotropic state, which is obtained by applying an isotropic pressure on all the boundaries of the specimen with a small initial friction coefficient. The particles will rearrange themselves to comply with the isotropic confining boundary pressure. The fabric components in the generated assembly are checked to ensure that a quasi-isotropic state is obtained in every tested specimen.

Case 1: Monodisperse random packing (2D)

A monodisperse granular packing with 1787 particles (the radius is 0.1m, the initial coefficient of friction is 0.1) is randomly generated in a square container and isotropically consolidated to a uniform stress state of 1MPa. The learning rate α and parameter β are taken as 0.01 and 0.03, respectively. After 5 iterations with 16 groups of numerical models performed, the macroscopic Young's modulus can be effectively predicted within an error of 1%. It takes 4.55 hours to perform the tests on a computer CPU: AMD A8-6600K, RAM:16G. The same computer configuration is used for all the four cases in this study. Note that the computed Poisson's ratio is larger than 0.5. Actually, the numerical Poisson's ratio is different from a physical one as it incorporates compensations for simplification factors such as contact formulations, roughness, and even particle shape.

Case 2: Monodisperse random packing (3D)

A monodisperse granular packing with 9167 particles (the radius is 0.1m, the initial coefficient of friction is 0.2) is randomly generated in a cubic container and isotropically consolidated to a uniform stress state of 1MPa. Both macroscopic Young's modulus and Poisson's ratio are calibrated in this case. The learning rate α and parameter β are taken as 0.03 and 0.05, respectively. After the 6^{th} iteration, the macroscopic Young's modulus can be predicted within an accuracy of 1% (the CPU time required is 11.65 hours), and after 13 iterations with 40 groups of numerical models performed, both Young's modulus and Poisson's ratio can be estimated within an accuracy of 1% (the computational time required is about

25.17 hours). The iterative process is shown in Fig.11.

Case 3: Polydisperse random packing (2D)

A polydisperse granular packing with 1655 particles (the radius is 0.1m, the initial coefficient of friction is 0.1) is randomly generated in a square container and isotropically consolidated to a uniform stress state of 1MPa. The learning rate α and parameter β are taken as 0.01 and 0.03, respectively. After 4 iterations with 13 numerical models performed, the macroscopic Young's modulus can be effectively predicted within an accuracy of 1% (the CPU time required is 5.58 hours).

It should be mentioned that only Young's modulus is calibrated in the two-dimensional cases, as it seems hard to calibrate both Young's modulus and Poisson's ratio at the same time in these cases. The reasons for the poor convergence experienced when calibrating both Young's modulus and Poisson's ratio simultaneously may be attributed to: (1) the 2D formulae still continue using the expression developed from the interactions in three-dimensional spheres; (2) the simplification of the tangential stiffness formula in the Hertz-Mindlin law. A detailed

investigation of interactions between non-linear elastic contacts (especially in 2D case) is out of the scope of this study but will be pursued in the future.

Case 4: Polydisperse random packing(3D)

A polydisperse granular packing with 7386 particles (the radius is 0.1m, the initial coefficient of friction is 0.2) is randomly generated in a cubic container and isotropically consolidated to a uniform stress state of 1MPa. Both macroscopic Young's modulus and Poisson's ratio are calibrated in this case. The learning rate α and parameter β are taken as 0.1 and 0.03, respectively. After 4 iterations with 13 groups of numerical models performed, the macroscopic Young's modulus can be predicted within an accuracy of 2% and the Poisson's ratio is predicted within 1% (the CPU time is 10.7 hours). Further iterations, however, cannot improve the solution accuracy anymore due to the highly non-linear and random nature of granular packings. Considering the measurement precision in experiments, the achieved prediction errors are acceptable. The iterative process is shown in Fig.11.

Figure 11 exhibits the evolutionary histories of the cost function during the iterative process for all four cases. Clearly, the cost function is not monotonically decreasing, due to nonlinear and discontinuous features of the relationship between the particle-scale contact stiffnesses and the macroscopic material properties. However, the cost function in all the cases exhibits a significant decrease from a relatively large initial value to a relatively small value (around 1×10^{-4}). The corresponding errors of Young's modulus decrease from 10%~20% to 1% or 2%. The tests show that the proposed framework can be used to estimate particle-level Hertz-type contact parameters for both monodisperse and polydisperse packings.

6 Illustration of nonlinear features of micro-macro relations in a granular system

Although the non-linear features of the micro-macro relationship in granular materials have been discussed in some existing research (Goldenberg, et al.[36], Hicher and Chang[60]), a clear

understanding of the Hertz-type based granular models is still lacking. In this section, the micro-macro relation in a numerical granular system based on the Herz-Mindlin contact law is visualised to illustrate its highly nonlinear features.

400 groups of models are simulated with the input parameters in Case 2 presented in Section 5.2 as a basis. The microscopic parameters (particle shear modulus and Poisson's ratio) are selected by picking the optimal microscopic set that has been obtained as the initial point and its surrounding parameters with uniformly spaced to a maximum relative variation of 1%. Except for the minor changes of the particle modulus and Poisson's ratio, the other input parameters or initial conditions keep the same. 9167 monodisperse particles are involved for each model with a porosity of around 0.3 (without considering the overlap amid particles).

The simulation results are presented in Figs. 12-14 with the fitted surfaces to show the micromacro relationships. Figs.12 and 13 display the macroscopic Young's modulus and Poisson's ratio normalised by the target Young's modulus and Poisson's ratio given in Section 5.2, respectively, against the particle-scale Hertz-Mindilin parameters. Fig.14 shows the logarithmic cost function (defined by Eq. (22)) against the Hertz-Mindilin contact parameters. These figures clearly demonstrate that the relationship between the micro and macro parameters in DEM is highly nonlinear with many local optima and noisy gradients.

It should be mentioned that Figs. 12-14 are just approximated visualisations. If a narrower microscopic parameter space is adopted, the fitted surfaces will be different. However, the current 'resolution' is able to provide useful explanations why a common optimisation algorithm, such as the gradient descent, is difficult to minimise the loss function in order to obtain satisfactory calibration parameters. In addition, the surrogate models are widely used to calibrate DEM parameters (Richter, et al.[73], Nguyen, et al.[74]). Figs. 12-14 may support an implication that only the surrogate model with a narrow parameter space is capable of

predicting macroscopic input parameters with high accuracy, for the Hertz-type based DEM models.

7 Conclusion

A combined analytical-computational method has been proposed to calibrate the Hertz-type contact parameters for DEM simulation. Based on Reuss's hypothesis and empirical simulations, a set of semi-analytical and semi-empirical formulae linking particle-scale contact parameters to macroscopic deformation parameters are derived for both 2D and 3D models. These formulae are taken as initial inputs for the following auto-trainings by using a wellknown machine learning algorithm - adaptive moment estimation and then much-improved predictions of microscopic parameters are obtained.

The proposed framework is tested with randomly generated monodisperse and polydisperse packings in both 2D and 3D cases. The results show that the refined particle-scale contact parameters are able to match the macroscopic elastic modulus within an error of 1~2% after a few iterations. The total computational costs involved, however, depends on selecting a reasonable learning rate. This issue is worth being pursued further to make the calibration procedure more effective.

It should be emphasised that both of the initial analytical solutions and the following optimisation algorithm is indispensable for a successful calibration in the proposed framework. Without a relatively accurate initial guess, the optimisation algorithm suffers from unpredictable local optimums and slow convergence. On the other hand, without the use of optimisation algorithms, the derived continuum-based analytical solution only provides a lowlevel approximation to the actual parameters.

Appendix: Stress-strain relationship of granular material

(1) Micromechanical definition of stress

Stress is a continuum quantity and therefore does not exist at the pore spaces in a particle assembly. To link the macroscopic stress to particle-scale contact forces, averaging procedures are necessary. The increments of the average stress tensor $\Delta\sigma_{ij}$ in a control volume V is well derived with a scheme of averaging contact forces of particles in the volume (Chang, et al.[26], Christoffersen, et al.[69]):

$$\Delta\sigma_{ij} = \frac{1}{V}\sum_{c=1}^{N_c} \Delta f^c L^c_j \tag{32}$$

where L^c_j is the *branch vector* (vector connecting centroids of particles in the *c-th* contact). In the case that a quasi-static loading state is used in DEM models, the Eq. (32) complies with the uniformity assumptions of Caillerie (Caillerie[70], Wang, et al.[71]) and therefore the secondary terms of the calculated stress tensor are negligible.

(2) Micro-macro relationship based on the static hypothesis

Since the Hertz-type contact stiffnesses are pressure-dependent, the static hypothesis is introduced to derive the stress-strain relationships considering that the Hertz-type contact stiffness at any given stress conditions can be easily determined by static hypothesis. (Yimsiri and Soga[30]).

By using the static hypothesis, the particle contact forces can be approximated by the mean stress of the packing structure as (Chang, et al.[26], Chang and Liao[29]).

$$\Delta f_i^c = \sigma_{ij} A\, n_{jkk}^c \ (i, j, k=1,2,3) \tag{33}$$

where the tensor A_{jk} is a parameter associated with the particle structure and will be determined subsequently; and n_k^c is the unit outward normal vector at the contact interface.

The inter-particle force formulation obtained from the static hypothesis must be consistent with the pre-stated definition of stress for a granular packing. Substituting Eq. (32) into Eq. (33) gives rise to:

$$\left(\frac{1}{V}\sum_{c=1}^{N_c} L\, n\, A_{ickc}\right)_{jk} = \delta_{ij} \tag{34}$$

where N_c is the total number of interparticle contacts in volume V and δ_{ij} is the Kronecker tensor. Then the tensor A_{jk} can be given as:

$$A_{jk} = \left[\frac{1}{V}\sum_{c=1}^{N_c} L\, n_{jckc}\right]^{-1} \tag{35}$$

(3) Micromechanical description of strain

The strain tensor ε_{ij} can be defined by the principle of energy conservation. Without considering the work of body forces of particles, the external work done to the assembly is equal to the internal work done over all interparticle contacts in volume V:

$$\frac{1}{V}\sum_{c=1}^{N_c} \Delta f\, u_{icic} = \Delta\sigma\varepsilon_{ijij} \tag{36}$$

By substituting Eq. (33) into Eq. (36),

$$\Delta\sigma\, \varepsilon_{ij}\left(\delta_{ij} - \frac{1}{V}\sum_{c=1}^{N_c} u\, A\, n_{ic\,jk}\, n_{kc}\right) = 0 \tag{37}$$

Since the stress increments $\Delta\sigma_{ij}$ can be arbitrarily given, the strain tensor ε_{ij} can be described as:

$$\varepsilon_{ij} = \frac{1}{V}\sum_{c=1}^{N_c} u_i^c A_{jk}^c n_k^c \tag{38}$$

Note that the current strain definition is not unique in granular mechanics. More definitions for the average strain tensor can be found in (Bonelli, et al.[72]).

(4) Constitutive relationship and compliance tensor

According to the principle of solid mechanics, the stress-strain relations can be expressed with the compliance tensor S_{ijkl} as follows:

$$\varepsilon_{ij} = S_{ijkl}\sigma_{kl} \tag{39}$$

By combining Eqs. (4), (33) and (38), the compliance tensor can be expressed as:

$$S_{ijkl} = \frac{1}{V} A_{lmjn} \sum_{c=1}^{N^c} n_{ikn}^c s^c n_{m}^c \quad (i, j,k,l,m,n=1,2,3) \tag{40}$$

(5) Integral form of compliance tensor and stress-strain relationship

Under the condition that all particles are of equal size, the *branch vector* L^c_j can be rewritten as:

$$L^c_j = 2rn^c_j \tag{41}$$

where r is the radius of monodisperse particles.

For a granular assembly with a large number of particles and contacts, the orientations of contact normals can be assumed to obey a statistically even distribution. Eq. (40) can thus be expressed in a continuum form. Let the distribution density function of particle contacts be $\rho\theta$

ραβ( ) or (,), where θ is the angle in the polar coordinate system (2D, see Fig. 2) and α, β are the angles in the spherical coordinate system (3D, refer to Fig. 1). The density function of contacts represents the number of contacts that direct to a certain angle in space and therefore satisfies the condition:

$$\begin{cases} \int_0^{2\pi} \rho\theta\,\theta(\,)d = 1 & \text{(2D)} \\ \int_0^{2\pi}\int_0^{\pi} \rho\gamma\beta\,\gamma\gamma\beta(\,,)\sin\, d\, d = 1 & \text{(3D)} \end{cases} \tag{42}$$

The number of contacts in a local area $d\Omega$ is given as $N_c\rho\theta(\,)d\Omega$ or $N_c\rho\gamma\beta(\,,\,)d\Omega$, where N_c is the total number of contacts in the volume V.

Under the condition that the particle assembly is statistically isotropic or quasi-isotropic, the distribution density function should be a constant:

$$\begin{cases} \rho\theta(\,) = \dfrac{1}{2\pi} & \text{(2D)} \\ \rho\gamma\beta(\,,) = \dfrac{1}{4\pi} & \text{(3D)} \end{cases} \tag{43}$$

Replacing the summation in Eq. (35) by integration leads to:

$$A_{jk} = \begin{cases} \dfrac{rN_c}{\pi V}\int_0^{2\pi} n\,n\,d_{jk}\,\theta = \dfrac{rN_c}{2}\begin{bmatrix}1 & 0\\ 0 & 1\end{bmatrix} = \dfrac{rN_c}{2}\delta_{jk} & \text{(2D, } j,k=1,2) \\ \dfrac{rN_c}{3V}\begin{bmatrix}1 & 0 & 0\\ 0 & 1 & 0\\ 0 & 0 & 1\end{bmatrix} & \text{(3D)} \end{cases} \tag{44}$$

$$\frac{1}{4\pi}\int_0^{2\pi}\int_0^{\pi} n_j n_k \sin\gamma\gamma\beta d\,d = \frac{1}{4\pi}\cdot 2rN_c \cdot 00\ 0\ 1\ \ 1\ 0 = \frac{1}{4\pi}\cdot 2rN_c\,\delta_{jk} \quad \text{(3D, } j,k=1,2,3\text{)}$$

$$\frac{1}{4\pi}\cdot 2\pi V$$

Therefore the summation in Eq. (40) leads to:

$$S_{ijkl} = \frac{V}{\int_0^{2\pi}\int_0^{\pi}} \begin{cases} \dfrac{1}{4\pi}\cdot 2\pi r N_{2c}\,\delta\delta_{lmjn}\int_0 n_s n_d m_{ikn}\theta & \text{(2D)} \\ \dfrac{1}{16\pi r N_c}\cdot 9V^2\,\delta\delta_{lm}\ _{jn} n_s n_{mikc}\ _c\ _{nc}\sin\gamma\gamma\beta d\,d & \text{(3D)} \end{cases} \tag{45}$$

For isotropic fabric, $\delta\delta_{lm} = {}_{jn}1$ so that $l = m\ j, = n$. Eq. (45) becomes:

$$S_{ijkl} = \frac{V}{\int_0^{2\pi}\int_0^{\pi}} \begin{cases} \dfrac{1}{4\pi}\cdot 2\pi r N_{2c}\int_0 n_s n_d l_{ik}\ _j\theta & \text{(2D, } i,j = 1,2, k,l = 1,2\text{)} \\ \dfrac{1}{16\pi r N_c}\cdot 9V^2\,\delta\delta_{lm}\ _{jn} n_s n_{mikc}\ _c\ _{nc}\sin\gamma\gamma\beta d\,d & \text{(3D)} \end{cases} \tag{46}$$

$$\frac{1}{16\pi r N_c}\cdot 9V\ n_s n_l{}^c{}_{ik}{}^c\ {}^c{}_j\sin\gamma\gamma\beta d\ d \quad \text{(3D, , , , } i,j,k,l = 1,2,3\text{)}$$

By performing integration on Eq. (46), the stress-strain relationship under the small strain condition becomes:

2D case:

$$\begin{pmatrix} \varepsilon_{11} \\ \varepsilon_{22} \\ 2\varepsilon_{12} \end{pmatrix} = \frac{V}{8r N_c} \begin{bmatrix} a & b & \\ b & a & \\ & & c \end{bmatrix} \begin{pmatrix} \sigma_{11} \\ \sigma_{22} \\ \sigma_{12} \end{pmatrix} \tag{47}$$

$$\text{where } a = +\frac{3}{k_n} - \frac{1}{k_s},\ b = -\frac{1}{k_n} + \frac{1}{k_s},\ c = +\frac{1}{k_n} - \frac{3}{k_s}.$$

$$\text{where } a = +\frac{3}{k_n} - \frac{1}{k_s},\ b = -\frac{1}{k_n} + \frac{1}{k_s},\ c = +\frac{4}{k_n} - \frac{6}{k_s}.$$

3D case:

$$\begin{bmatrix}\varepsilon_{11}\\ \varepsilon_{22}\\ \varepsilon_{33}\\ 2\varepsilon_{23}\\ 2\varepsilon_{13}\\ 2\varepsilon_{12}\end{bmatrix} = \frac{3V}{20rN_c}\begin{bmatrix} a & b & b & & & \\ b & a & b & & & \\ b & b & a & & & \\ & & & c & & \\ & & & & c & \\ & & & & & c \end{bmatrix}\begin{bmatrix}\sigma_{11}\\ \sigma_{22}\\ \sigma_{33}\\ \sigma_{23}\\ \sigma_{13}\\ \sigma_{12}\end{bmatrix} \tag{48}$$

The stress-strain relation for an isotropic elastic solid is given as:

2D plane stress case :

$$\begin{bmatrix}\varepsilon_{11}\\ \varepsilon_{22}\\ 2\varepsilon_{12}\end{bmatrix} = \frac{1}{E}\begin{bmatrix} 1 & -\nu & \\ -\nu & 1 & \\ & & 2(1+\nu) \end{bmatrix}\begin{bmatrix}\sigma_{11}\\ \sigma_{22}\\ \sigma_{12}\end{bmatrix} \tag{49}$$

2D plane strain case:

$$\begin{bmatrix}\varepsilon_{11}\\ \varepsilon_{22}\\ 2\varepsilon_{12}\end{bmatrix} = \frac{(1+\nu)}{E}\begin{bmatrix} 1-\nu & \nu & \\ \nu & 1-\nu & \\ & & 2 \end{bmatrix}\begin{bmatrix}\sigma_{11}\\ \sigma_{22}\\ \sigma_{12}\end{bmatrix} \tag{50}$$

3D case:

$$\begin{bmatrix}\varepsilon_{11}\\ \varepsilon_{22}\\ \varepsilon_{33}\\ 2\varepsilon_{23}\\ 2\varepsilon_{13}\\ 2\varepsilon_{12}\end{bmatrix} = \frac{1}{E}\begin{bmatrix} 1 & -\nu & \nu & & & \\ -\nu & 1 & -\nu & & & \\ \nu & -\nu & 1 & & & \\ & & & 2(1+\nu) & & \\ & & & & 2(1+\nu) & \\ & & & & & 2(1+\nu) \end{bmatrix}\begin{bmatrix}\sigma_{11}\\ \sigma_{22}\\ \sigma_{33}\\ \sigma_{23}\\ \sigma_{13}\\ \sigma_{12}\end{bmatrix} \tag{51}$$

The analytical solution of small strain modulus and Poisson's ratio of an isotropic granular assembly can be determined by comparing Eqs. (47-48) with Eqs. (49-51) as 2D plane stress case:

$$E = \frac{k(_n+3)k_s}{k_n+^1k_s}, \quad \frac{V k(_n+k_s)}{}, G= \frac{}{} \tag{52}$$

2D plane strain case:

$$E = \frac{2N r^2(3k+k k k)}{k(_n+k_s)}_c \quad \frac{k-k}{}_{ns2\,n\,s}, \nu = \frac{}{2k^{n^n}+2^sk_s}, G= \frac{2N r k k^2}{V k(_{cn}+k_{n\,s_s})} \tag{53}$$

3D model:

$$E = \frac{20N r k k^2 k k - 10N r k k^2}{8N r k k_{c\,2\,n\,s}}_{c\,n\,s}, \nu = \frac{}{k_n-k_s}_{n\,s}, G= \frac{}{2N r k k_{c\,2\,n\,s}} \tag{54}$$

(6) Small-strain modulus based on Hertz-Mindlin-type contact relations

For an isotropic elastic assembly under isotropic stress conditions (say the confining stress is σ_c), no shear stress is present in the isotropic elastic body and thus no tangential force occurs at the contacts. Recalling the static hypothesis, the normal contact forces at all contacts are of the same magnitude (Yimsiri and Soga[30]). With Eqs. (33) and (44), we can determine:

$$f_n = \frac{3V}{2rN_c}\sigma_c \tag{55}$$

By combining Eqs. (2)-(3), (46) and (55), the contact stiffnesses in both 2D and 3D model become:

---

[1] $V k(2_n+3)k_s \quad 2k_n+3k_s \quad 3(3V k_n+2)k_s$

where E, ν and G are the equivalent elastic constants of the granular packing.

$$k_n = \left(\frac{9VG_*^2}{2N_c(1-\nu)}\right)^{1/3} \sigma_c^{\frac{1}{3}} = \left[36V(1-\nu^*)G^{*2}\sigma_c\right]^{\frac{1}{3}} \tag{56}$$

$$k_s = \frac{N_c}{(2-\nu)}$$

Although the solutions in plane strain and plane stress cases are slight different, the difference is small. In this study, only the plane stress solutions are used to derive the analytical expressions for 2D models.

The small-strain modulus can be expressed as a function of isotropic confining stress:

2D case:

$$E = \frac{(8-7\nu_*)}{V}\left(\frac{N G_*}{c}\right)^{\frac{2}{3}} \left(\frac{8r_2}{c}\right)^{\frac{1}{3}} \left[36(1-\nu_*)\sigma_c\right]^{\frac{1}{3}} \tag{57}$$

$$\nu = \frac{\nu^*}{8-7\nu^*} \tag{58}$$

$$G = (4-3\nu)\left(\frac{2r_2}{V_c}\right)^{\frac{2}{3}} \left(\frac{N G_*}{*}\right)^{\frac{1}{3}} \left[36(1-\nu_*)\sigma_c\right]^{\frac{1}{3}} \tag{59}$$

3D case:

$$E = \left(\frac{20r_2}{(5-4\nu)V}\right)^{\frac{2}{3}} \left(\frac{e}{*}\right)^{\frac{1}{3}} \left(\frac{e}{6}\right)^{\frac{1}{3}} \left[G_*N\right]^{\frac{1}{3}} \left[(1-\nu_*)\sigma_3\right]^{\frac{1}{3}} \tag{60}$$

$$\nu = \frac{\nu^*}{10 - 8\nu^*} \tag{61}$$

$$G = \frac{20r^2 \left(G_* N_c \left(\sigma_3 (1-\nu_*)\sigma_c\right)^{\frac{1}{2}}\right)^{\frac{2}{3}}}{(10-7\nu)\, V \left(6\right)^{\frac{1}{3}}} \tag{62}$$

Note that the Poisson' ratio in Eq. (61) is already derived in the literature (Yimsiri and Soga[30]). The derived equivalent Poisson's ratio is irrelevant to the confining stress in Eqs. (58) and (61), which is actually not consistent with the physical intuition of granular material. The difference is partly due to the simplification of the tangential stiffness formulation.

References

1. Bourrier F, Nicot F, Darve F. Physical processes within a 2D granular layer during an impact. *Granular Matter* 2008;10(6):415-437.
2. Sibille L, Donzé F-V, Nicot F, Chareyre B, Darve F. From bifurcation to failure in a granular material: a DEM analysis. *Acta Geotechnica* 2008;3(1):15.
3. Nicot F, Sibille L, Darve F. Failure in rate-independent granular materials as a bifurcation toward a dynamic regime. *International Journal of Plasticity* 2012;29:136-154.
4. Wang M, Feng Y, Wang C. Coupled bonded particle and lattice Boltzmann method for modelling fluid–solid interaction. *International Journal for Numerical and Analytical Methods in Geomechanics* 2016;40(10):1383-1401.
5. Wang M, Feng Y, Pande G, Zhao T. A coupled 3-dimensional bonded discrete element and lattice Boltzmann method for fluid-solid coupling in cohesive geomaterials. *International Journal for Numerical and Analytical Methods in Geomechanics* 2018;42(12):1405-1424.
6. Liu J, Nicot F, Zhou W. Sustainability of internal structures during shear band forming in 2D granular materials. *Powder technology* 2018;338:458-470.
7. Qu T, Wang S, Fu J, Hu Q, Zhang X. Numerical Examination of EPB Shield Tunneling–Induced Responses at Various Discharge Ratios. *Journal of Performance of Constructed Facilities* 2019;33(3):04019035.
8. Wang S, Qu T, Fang Y, Fu J, Yang J. Stress Responses Associated with Earth Pressure Balance Shield Tunneling in Dry Granular Ground Using the Discrete-Element Method. *International Journal of Geomechanics* 2019;19(7):04019060.
9. Cambou B, Darve F, Nicot F. Particle methods in geomechanics. *International Journal for Numerical and Analytical Methods in Geomechanics* 2019;43(5):831-832.
10. Wautier A, Bonelli S, Nicot F. DEM investigations of internal erosion: Grain transport in the light of micromechanics. *International Journal for Numerical and Analytical Methods in Geomechanics* 2019;43(1):339-352.
11. Dugelas L, Coulibaly JB, Bourrier F, et al. Assessment of the predictive capabilities of discrete element models for flexible rockfall barriers. *International Journal of Impact Engineering* 2019;133:103365.

12. Qu T, Wang S, Hu Q. Coupled Discrete Element-Finite Difference Method for Analysing Effects of Cohesionless Soil Conditioning on Tunneling Behaviour of EPB Shield. *KSCE Journal of Civil Engineering* 2019;23(10):4537-4551.
13. Gao G, Meguid M. Effect of particle shape on the response of geogrid-reinforced systems: Insights from 3D discrete element analysis. *Geotextiles and Geomembranes* 2018;46(6):685-698.
14. Gao G, Meguid M. On the role of sphericity of falling rock clusters—insights from experimental and numerical investigations. *Landslides* 2018;15(2):219-232.
15. Coetzee CJ. Calibration of the discrete element method and the effect of particle shape. *Powder Technology* 2016;297:50-70.
16. Coetzee CJ. Review: Calibration of the discrete element method. *Powder Technology* 2017;310:104-142.
17. Qu T, Feng Y, Wang Y, Wang M. Discrete element modelling of flexible membrane boundaries for triaxial tests. *Computers and Geotechnics* 2019;115:103154.
18. O'Sullivan C. *Particulate discrete element modelling: a geomechanics perspective*. CRC Press; 2014.
19. Satake M. A discrete-mechanical approach to granular materials. *International journal of engineering science* 1992;30(10):1525-1533.
20. Bagi K. Stress and strain in granular assemblies. *Mechanics of materials* 1996;22(3):165177.
21. Liao C-L, Chang T-P, Young D-H, Chang CS. Stress-strain relationship for granular materials based on the hypothesis of best fit. *International Journal of Solids and Structures* 1997;34(31-32):4087-4100.
22. Kruyt NP, Rothenburg L. Statistical theories for the elastic moduli of two-dimensional assemblies of granular materials. *International journal of engineering science* 1998;36(10):1127-1142.
23. Chang CS, Lun M. Elastic material constants for isotropic granular solids with particle rotation. *International journal of solids and structures* 1992;29(8):1001-1018.
24. Digby P. The effective elastic moduli of porous granular rocks. *Journal of Applied Mechanics* 1981;48(4):803-808.
25. Walton K. The effective elastic moduli of a random packing of spheres. *Journal of the Mechanics and Physics of Solids* 1987;35(2):213-226.
26. Chang CS, Chao SJ, Chang Y. Estimates of elastic moduli for granular material with anisotropic random packing structure. *International journal of solids and structures* 1995;32(14):1989-2008.
27. Chou P, Carleone J, Hsu C. Elastic constants of layered media. *Journal of composite materials* 1972;6(1):80-93.
28. Li X, Yu H, Li X. Macro–micro relations in granular mechanics. *International Journal of Solids and Structures* 2009;46(25-26):4331-4341.
29. Chang CS, Liao CL. Estimates of elastic modulus for media of randomly packed granules. *Applied Mechanics Reviews* 1994;47(1S):S197-S206.
30. Yimsiri S, Soga K. Micromechanics-based stress strain behaviour of soils at small strains. *Geotechnique* 2000;50(5):559-671.
31. Liao CL, Chan TC, Suiker AS, Chang CS. Pressure-dependent elastic moduli of granular assemblies. *International Journal for Numerical and Analytical Methods in Geomechanics* 2000;24(3):265-279.

32. Zhu H, Nicot F, Darve F. Meso-structure organization in two-dimensional granular materials along biaxial loading path. *International Journal of Solids and Structures* 2016;96:25-37.
33. Zhu H, Nicot F, Darve F. Meso-structure evolution in a 2D granular material during biaxial loading. *Granular Matter* 2016;18(1):3.
34. Zhu H, Veylon G, Nicot F, Darve F. On the mechanics of meso-scale structures in twodimensional granular materials. *European Journal of Environmental and Civil Engineering* 2017;21(7-8):912-935.
35. Xiong H, Nicot F, Yin Z. A three - dimensional micromechanically based model. *International Journal for Numerical and Analytical Methods in Geomechanics* 2017;41(17):1669-1686.
36. Goldenberg C, Tanguy A, Barrat J-L. Particle displacements in the elastic deformation of amorphous materials: Local fluctuations vs. non-affine field. *EPL (Europhysics Letters)* 2007;80(1):16003.
37. Ouaguenouni S, Roux J-N. Force distribution in frictionless granular packings at rigidity threshold. *EPL (Europhysics Letters)* 1997;39(2):117-122.
38. Sun Q, Jin F, Liu J, Zhang G. Understanding force chains in dense granular materials. *International Journal of Modern Physics B* 2010;24(29):5743-5759.
39. Pouragha M, Duriez J, Wautier A, Wan R, Nicot F, Darve F. Preferential growth of force network in granular media. *Granular Matter* 2019;21(3):67.
40. Nicot F, Xiong H, Wautier A, Lerbet J, Darve F. Force chain collapse as grain column buckling in granular materials. *Granular Matter* 2017;19(2):18.
41. Goldenberg C, Goldhirsch I. Force chains, microelasticity, and macroelasticity. *Physical review letters* 2002;89(8):084302.
42. Goldenberg C, Goldhirsch I. Friction enhances elasticity in granular solids. *Nature* 2005;435(7039):188-191.
43. Yoon J. Application of experimental design and optimization to PFC model calibration in uniaxial compression simulation. *International Journal of Rock Mechanics and Mining Sciences* 2007;44(6):871-889.
44. Benvenuti L, Kloss C, Pirker S. Identification of DEM simulation parameters by Artificial Neural Networks and bulk experiments. *Powder technology* 2016;291:456-465.
45. Zhou H, Hu Z, Chen J, Lv X, Xie N. Calibration of DEM models for irregular particles based on experimental design method and bulk experiments. *Powder Technology* 2018;332:210-223.
46. Rackl M, Hanley KJ. A methodical calibration procedure for discrete element models. *Powder technology* 2017;307:73-83.
47. Boikov A., Savelev R., Payor V. DEM Calibration Approach: Random Forest, *Journal of Physics: Conference Series*, IOP Publishing, 2018, pp. 012009.
48. Pachón-Morales J, Do H, Colin J, Puel F, Perré P, Schott D. DEM modelling for flow of cohesive lignocellulosic biomass powders: Model calibration using bulk tests. *Advanced Powder Technology* 2019;30(4):732-750.
49. Do HQ, Aragón AM, Schott DL. A calibration framework for discrete element model parameters using genetic algorithms. *Advanced Powder Technology* 2018;29(6):1393-1403.
50. Cheng H, Shuku T, Thoeni K, Yamamoto H. Probabilistic calibration of discrete element simulations using the sequential quasi-Monte Carlo filter. *Granular matter* 2018;20(1):119.

51. Cheng H, Shuku T, Thoeni K, Tempone P, Luding S, Magnanimo V. An iterative Bayesian filtering framework for fast and automated calibration of DEM models. *Computer Methods in Applied Mechanics and Engineering* 2019;350(15):268-294.
52. Qu T, Feng YT, Zhao TT, Wang M. Calibration of Linear Contact Stiffnesses in Discrete Element Models Using a Hybrid Analytical-Computational Framework. *Powder Technology* 2019;356:795-807.
53. Kingma DP, Ba J. Adam: A method for stochastic optimization. *arXiv preprint arXiv:1412.6980* 2014;
54. Itasca, PFC3D—Particle Flow Code in 3 Dimensions, Version 5, Minneapolis, USA, 2014
55. Chang CS, Sundaram SS, Misra A. Initial moduli of particulated mass with frictional contacts. *International Journal for Numerical and Analytical Methods in Geomechanics* 1989;13(6):629-644.
56. Cundall P. Computer simulations of dense sphere assemblies. In: ed. *Studies in Applied Mechanics*. Elsevier; 1988: 113-123.
57. Tsuji Y, Tanaka T, Ishida T. Lagrangian numerical simulation of plug flow of cohesionless particles in a horizontal pipe. *Powder technology* 1992;71(3):239-250.
58. Hicher P-Y, Chang CS. Evaluation of two homogenization techniques for modeling the elastic behavior of granular materials. *Journal of engineering mechanics* 2005;131(11):1184-1194.
59. Zhu Q, Shao J-F, Mainguy M. A micromechanics-based elastoplastic damage model for granular materials at low confining pressure. *International Journal of Plasticity* 2010;26(4):586-602.
60. Hicher P-Y, Chang CS. Anisotropic nonlinear elastic model for particulate materials. *Journal of Geotechnical and Geoenvironmental Engineering* 2006;132(8):1052-1061.
61. Luding S. Granular media: Information propagation. *Nature* 2005;435(7039):159-160.
62. Peters JF, Muthuswamy M, Wibowo J, Tordesillas A. Characterization of force chains in granular material. *Phys Rev E Stat Nonlin Soft Matter Phys* 2005;72(4 Pt 1):041307.
63. Zhang J, Majmudar T, Sperl M, Behringer R. Jamming for a 2D granular material. *Soft Matter* 2010;6(13):2982-2991.
64. Gaspar N. A granular material with a negative Poisson's ratio. *Mechanics of Materials* 2010;42(7):673-677.
65. Gu X, Yang J. A discrete element analysis of elastic properties of granular materials. *Granular Matter* 2013;15(2):139-147.
66. Madsen K. A root-finding algorithm based on Newton's method. *BIT Numerical Mathematics* 1973;13(1):71-75.
67. Ruder S. An overview of gradient descent optimization algorithms. *arXiv preprint arXiv:1609.04747* 2016;
68. Feng Y, Zhao T, Kato J, Zhou W. Towards stochastic discrete element modelling of spherical particles with surface roughness: A normal interaction law. *Computer Methods in Applied Mechanics and Engineering* 2017;315:247-272.
69. Christoffersen J, Mehrabadi MM, Nemat-Nasser S. A micromechanical description of granular material behavior. *Journal of applied mechanics* 1981;48(2):339-344.
70. Caillerie D. Tenseur des contraintes dans un milieu granulaire. *Rapport d'activité Greco* 1991;771-775.
71. Wang R, Fu P, Zhang J-M, Dafalias YF. Deformation of granular material under continuous rotation of stress principal axes. *International Journal of Geomechanics* 2019;19(4):04019017.

72. Bonelli S, Millet O, Nicot F, Rahmoun J, De Saxcé G. On the definition of an average strain tensor for two-dimensional granular material assemblies. *International Journal of Solids and Structures* 2012;49(7-8):947-958.
73. Richter C, Rößler T, Kunze G, Katterfeld A, Will F. Development of a standard calibration procedure for the DEM parameters of cohesionless bulk materials–Part II: Efficient optimization-based calibration. *Powder Technology* 2020;360:967-976.
74. Nguyen T-T, André D, Huger M. Analytic laws for direct calibration of discrete element modeling of brittle elastic media using cohesive beam model. *Computational Particle Mechanics* 2019;6(3):393-409.

Figures

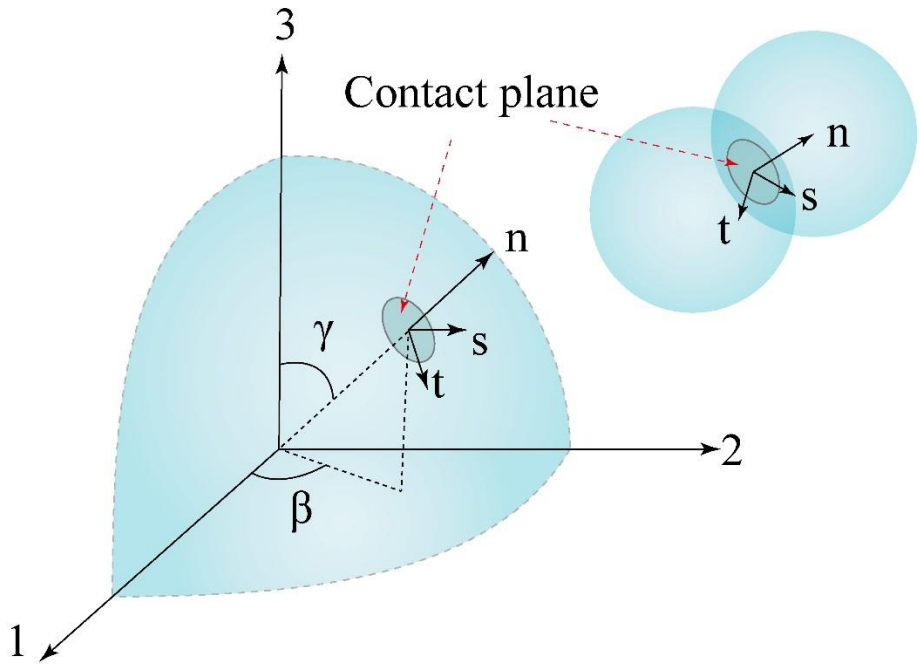

Fig.1 Spherical coordinate system and local system at c^{th} contact plane

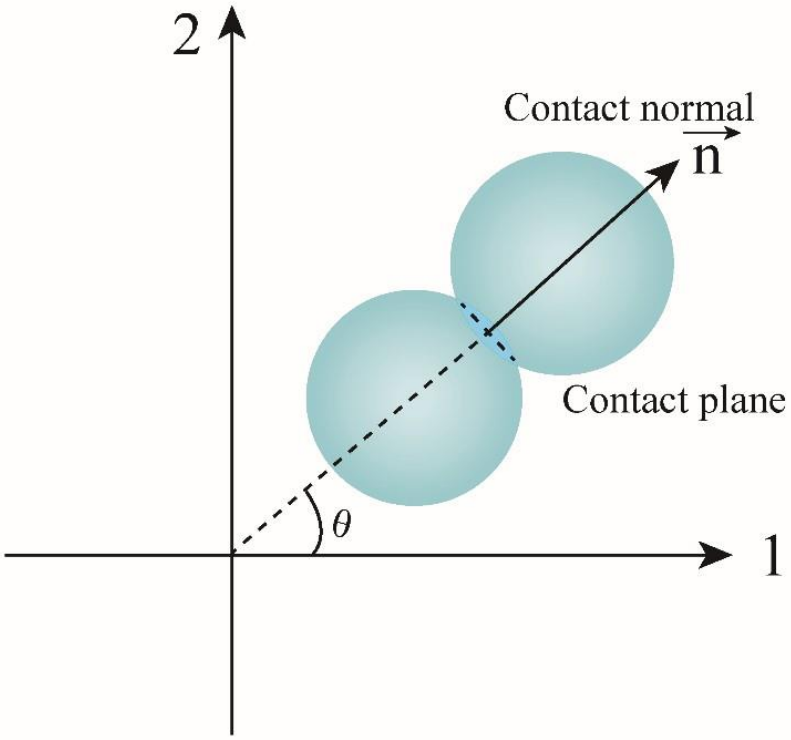

Fig. 2 Polar coordinate (2D) for directional distribution of inter-particle contact

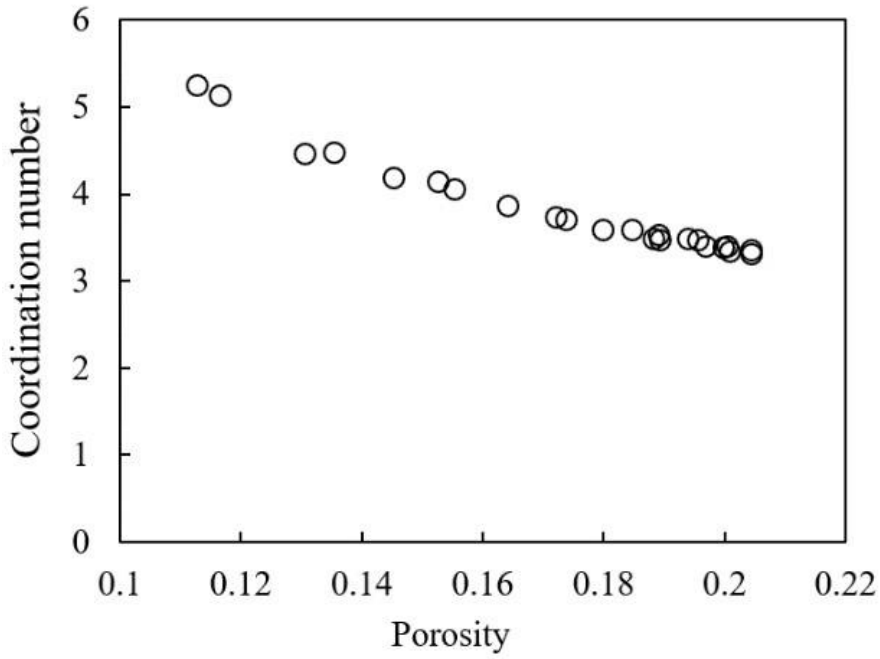

(a) 2D model

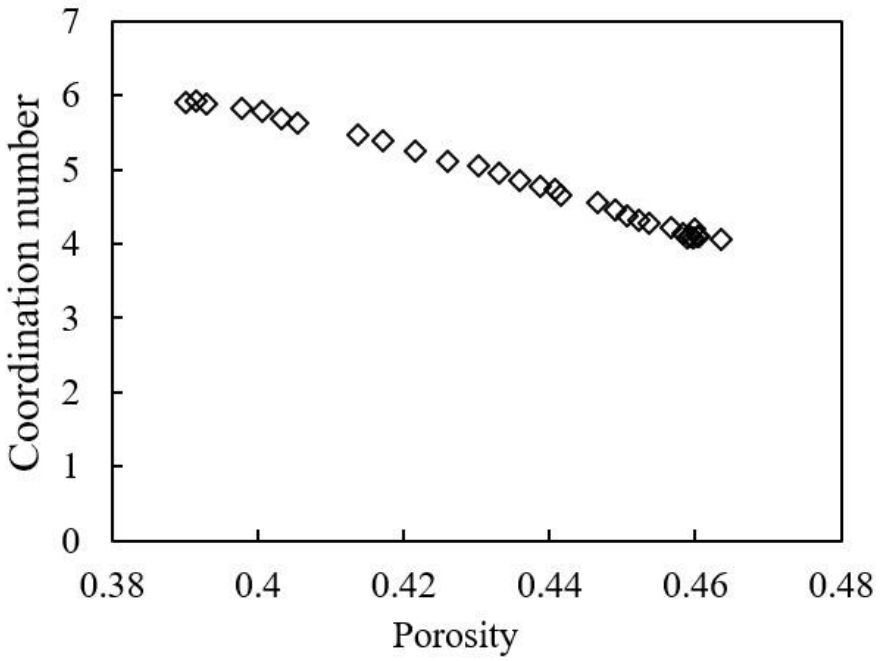

(b) 3D model

Fig.3 Porosity vs coordination number in used DEM packings (2D and 3D)

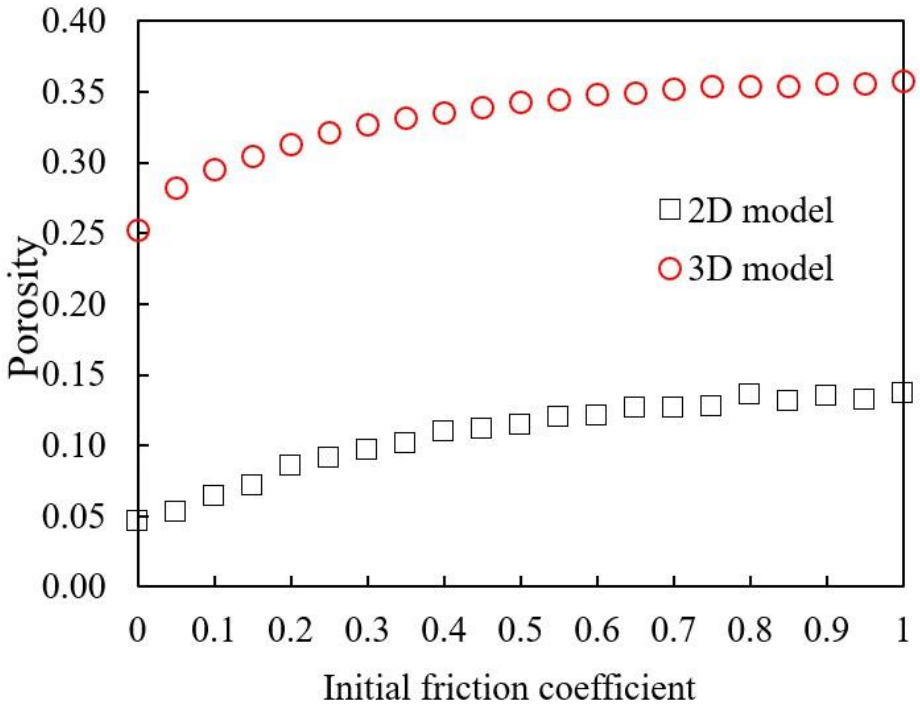

Fig.4 Initial coefficient of friction vs porosity in DEM packings

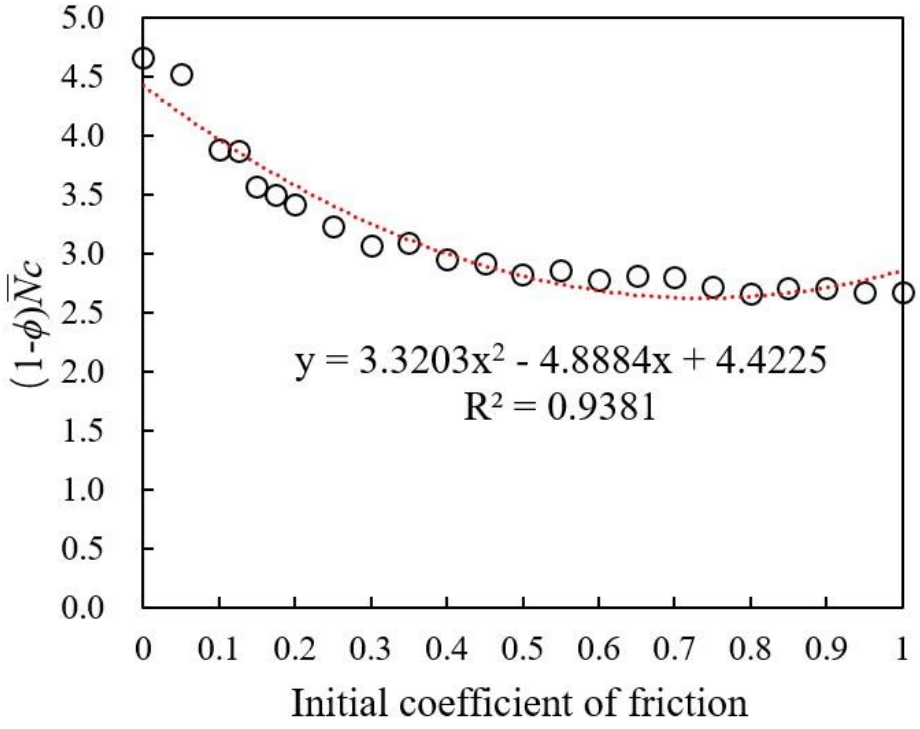

(a) 2D model

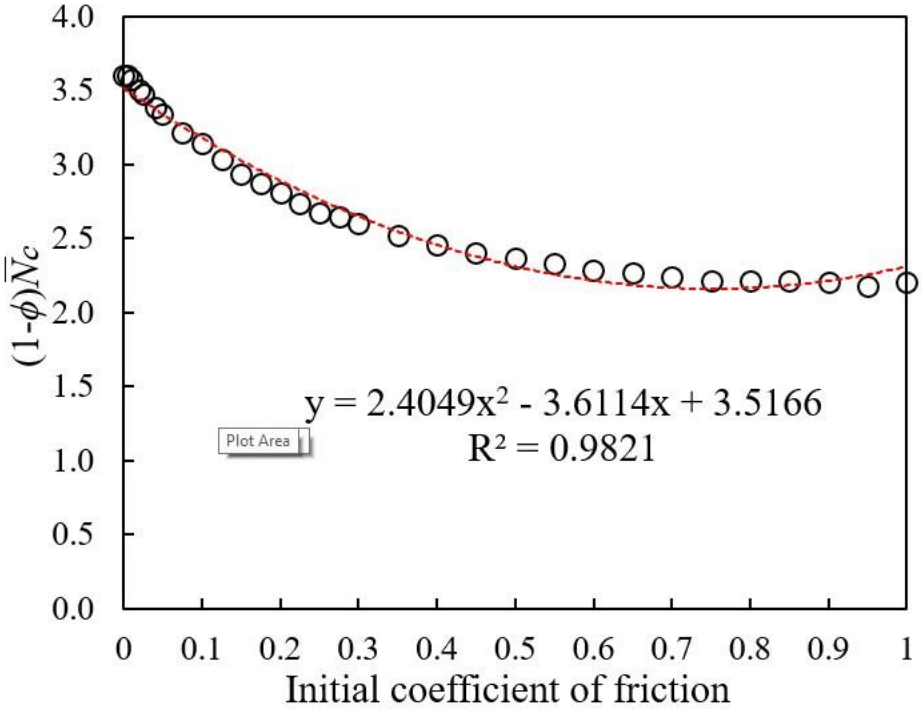

(b) 3D model

Fig. 5 Empirical relationship between initial coefficient of friction

and packing parameter $(1-)\varphi N_c$

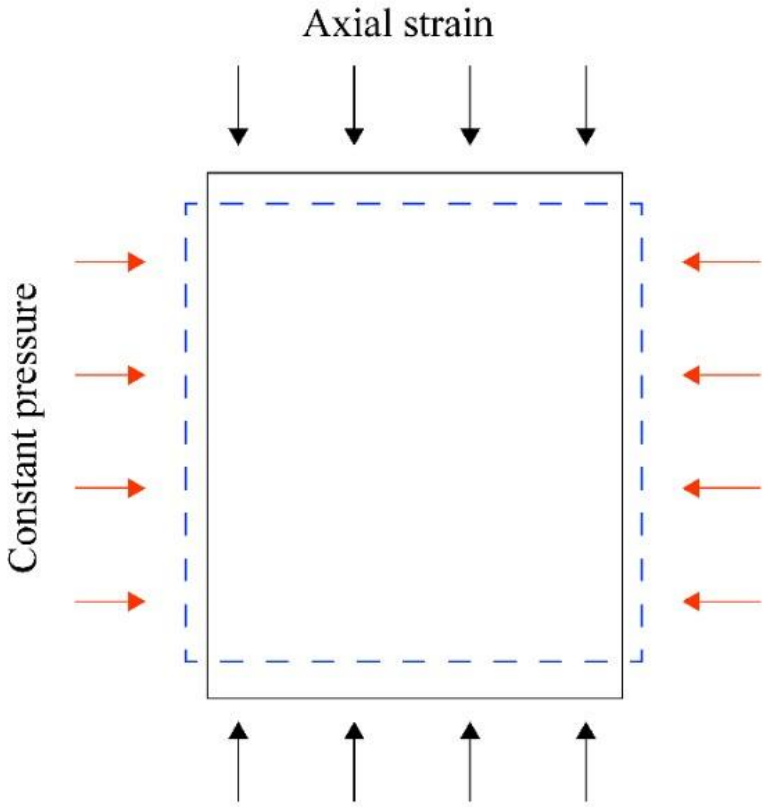

Fig.6 Schematic diagram for biaxial tests (2D and 3D)

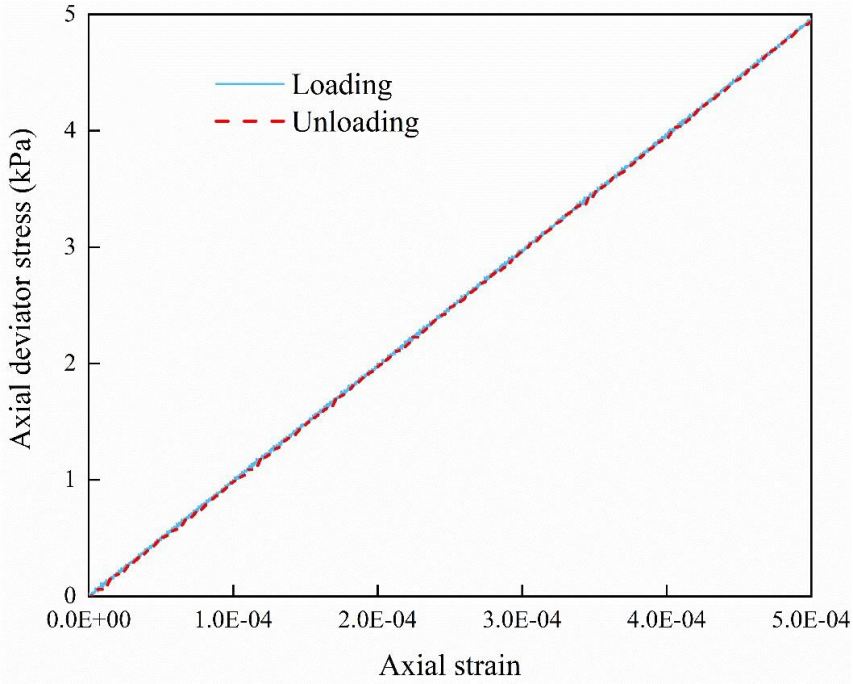

Fig.7 Axial deviatoric stress with respect to axial strain for load/unload tests

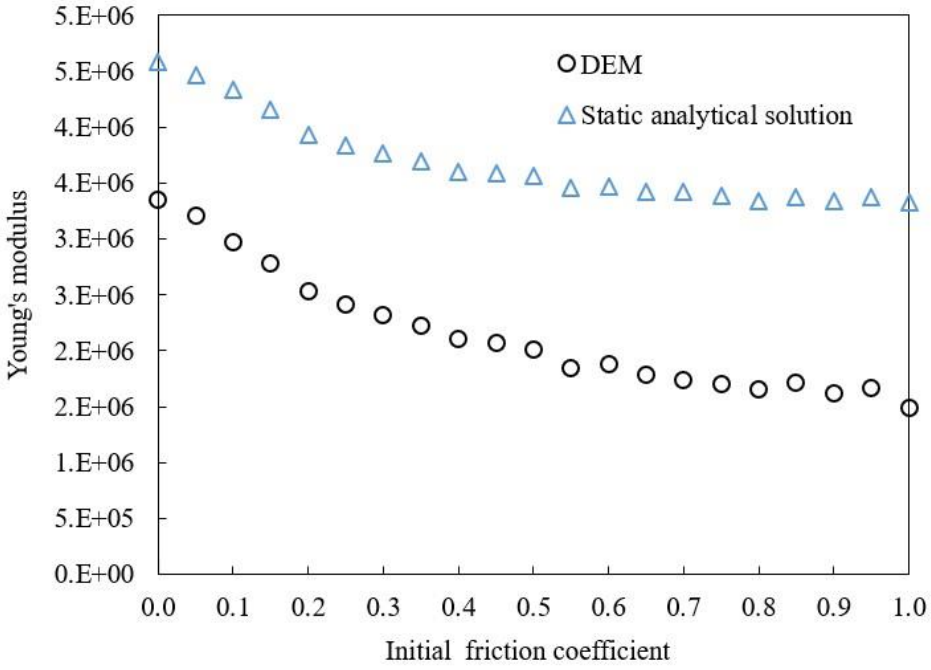

(a) 2D model

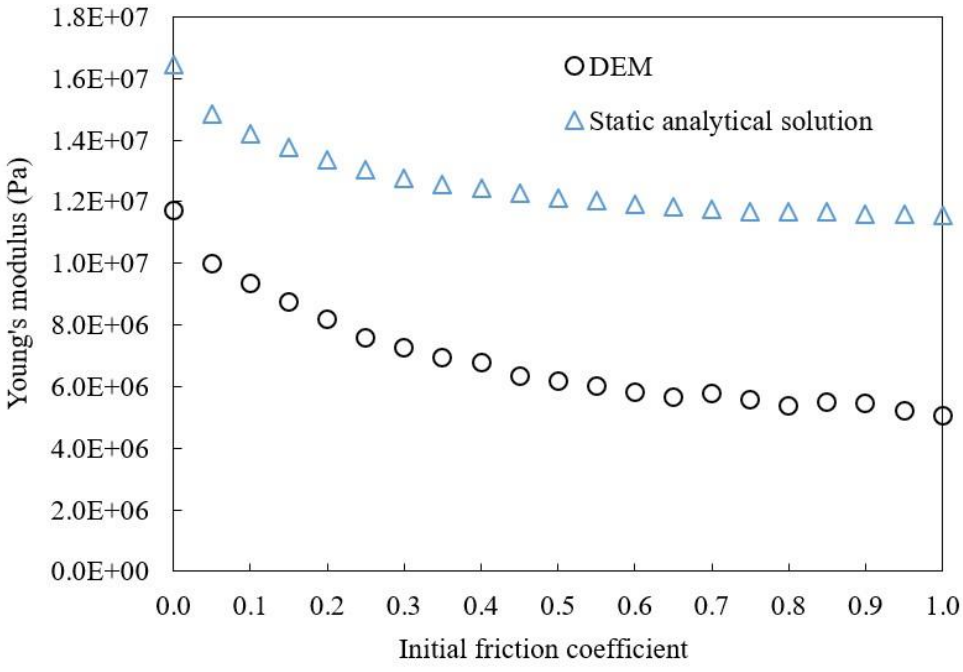

(b) 3D model

Fig.8 Comparision of macroscopic Young's modulus obtained by direct DEM simulations and static analytical solutions for different initial coefficients of friction

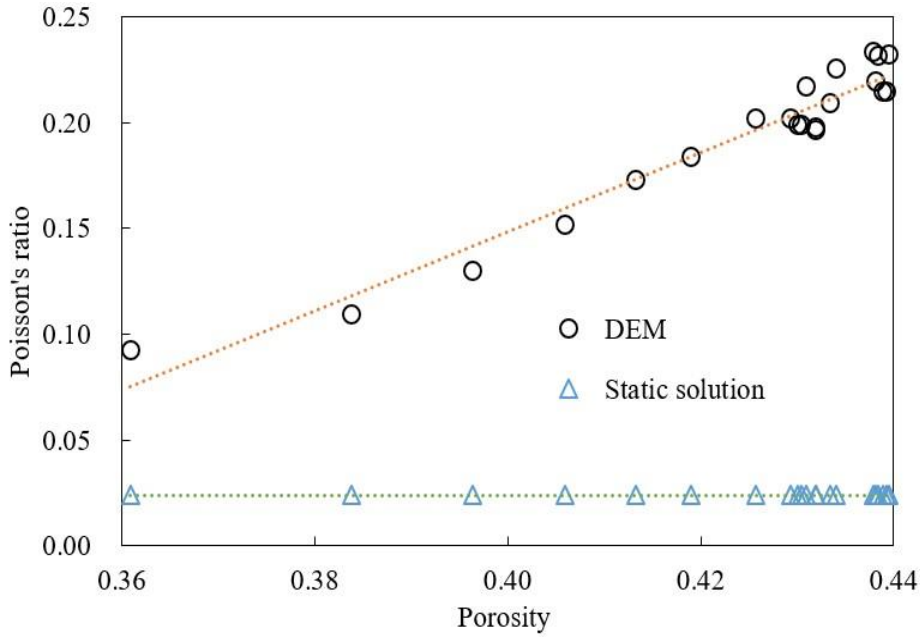

Fig.9 Comparision of macroscopic Possion's ratio obtained by direct DEM simulations and static analytical solutions for different porosities

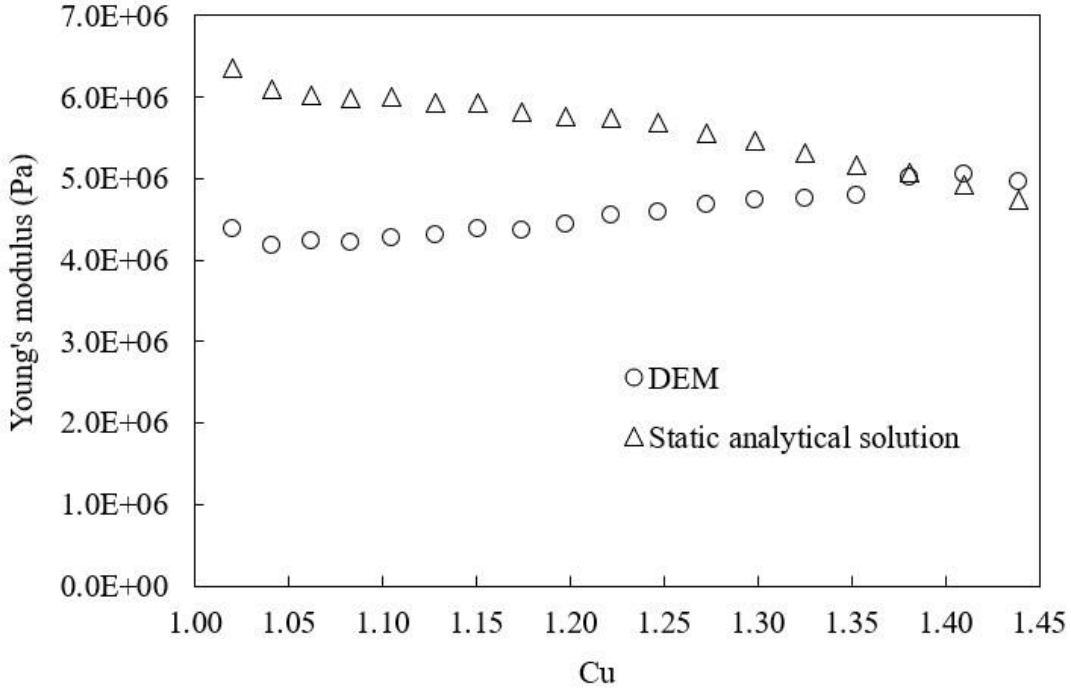

(a) 2D model

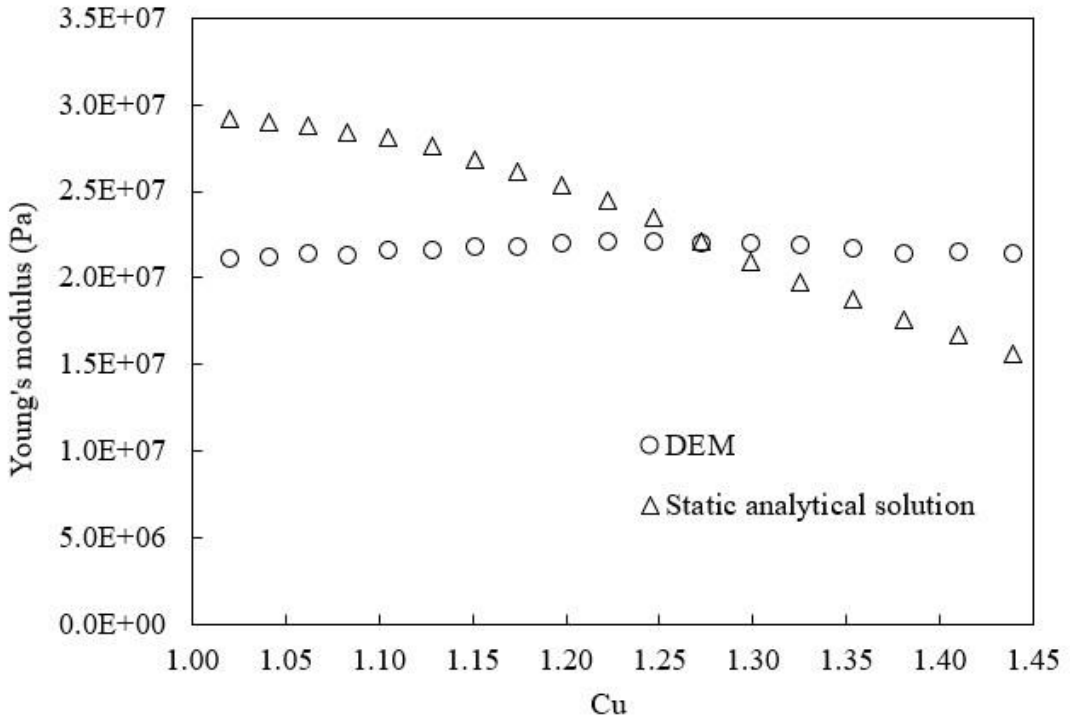

(b) 3D model

Fig.10 Macroscopic Young's modulus with respect to the coefficient of uniformity in granular packing (DEM simulations and static analytical solutions)

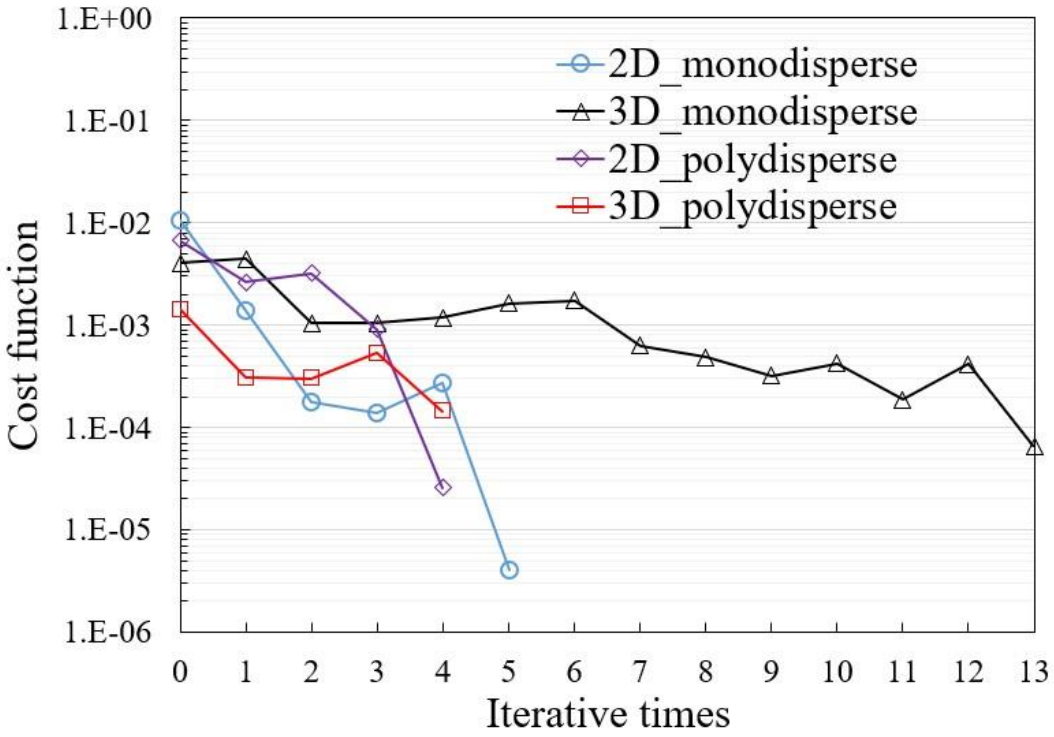

Fig.11 The convergent histories of the cost function for four test cases

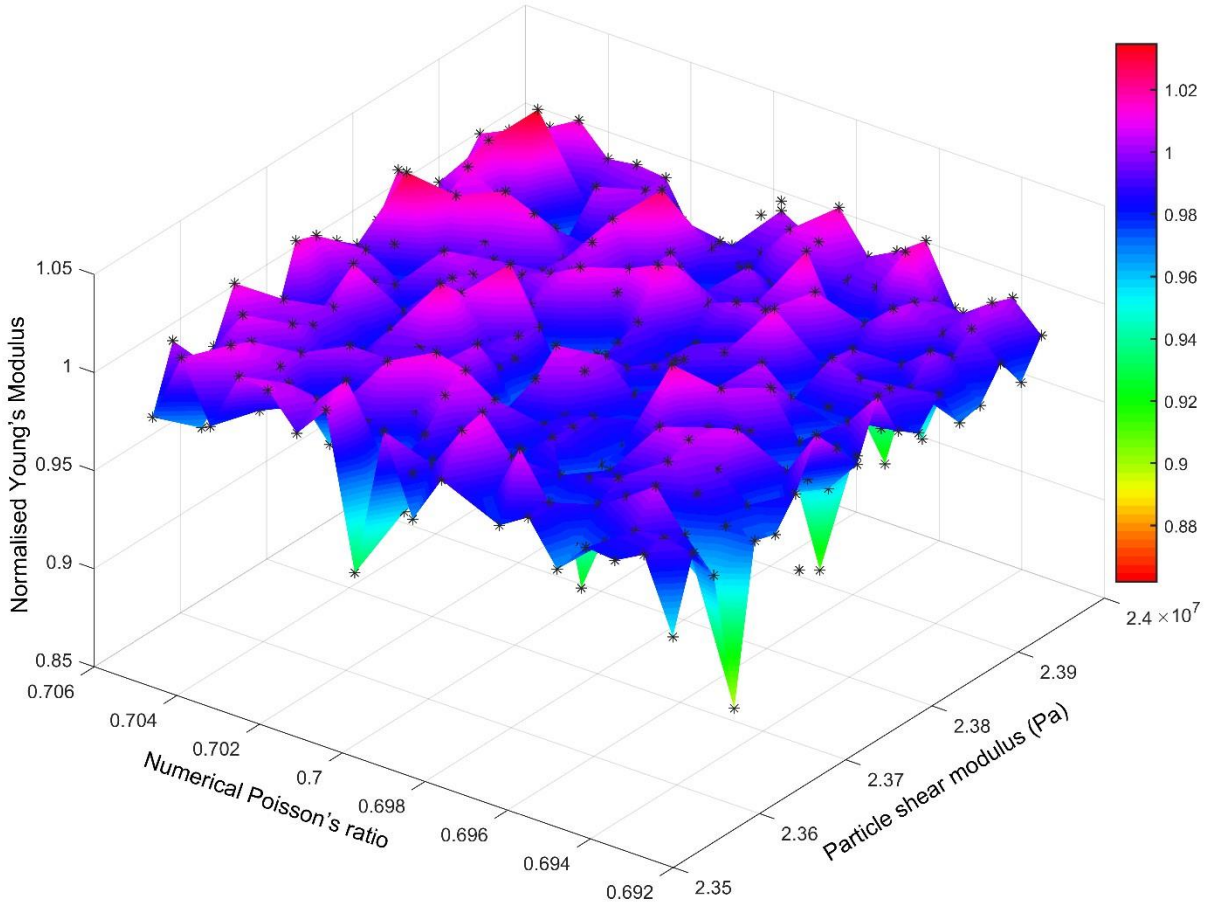

Fig. 12 A fitted surface of the normalised Young's modulus against Hertz-Mindilin contact parameters in a narrow parameter space for a 3D monodisperse packing

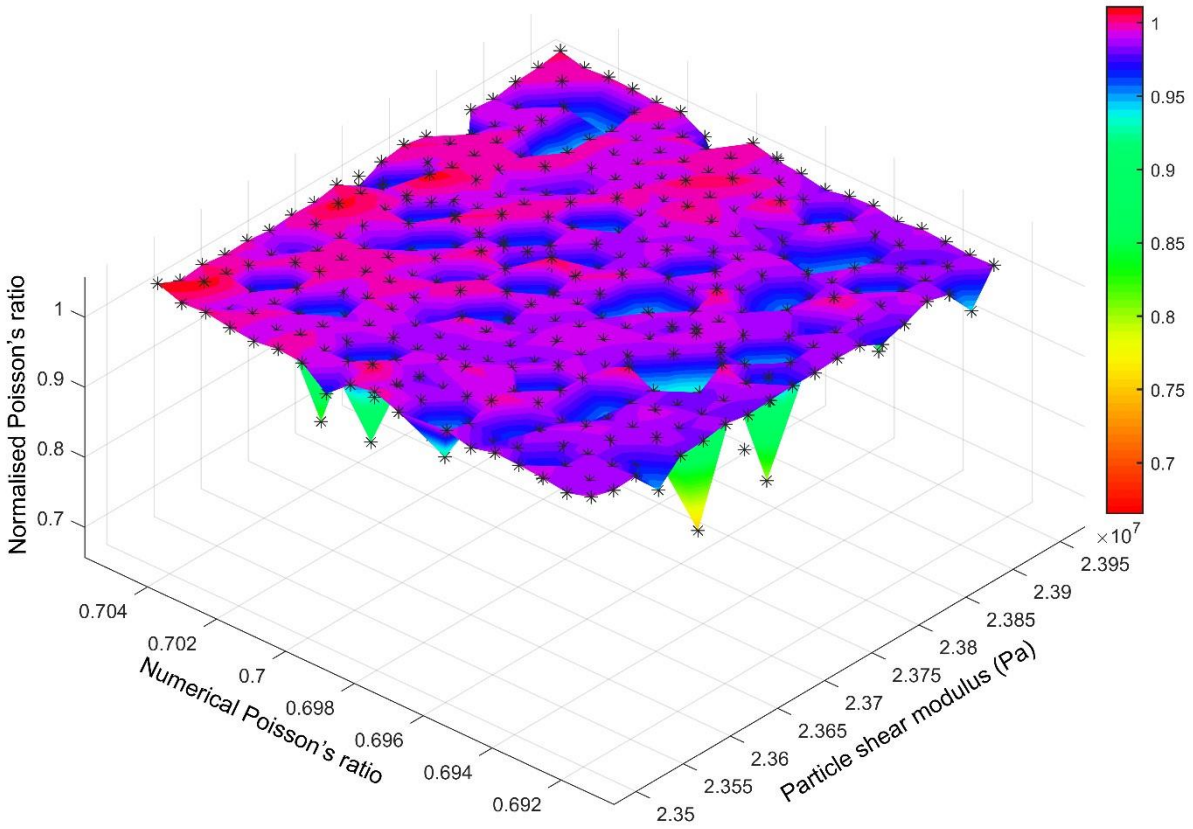

Fig. 13 A fitted surface of the normalised Poisson's ratio against Hertz-Mindilin contact parameters in a narrow parameter space for a 3D monodisperse packing

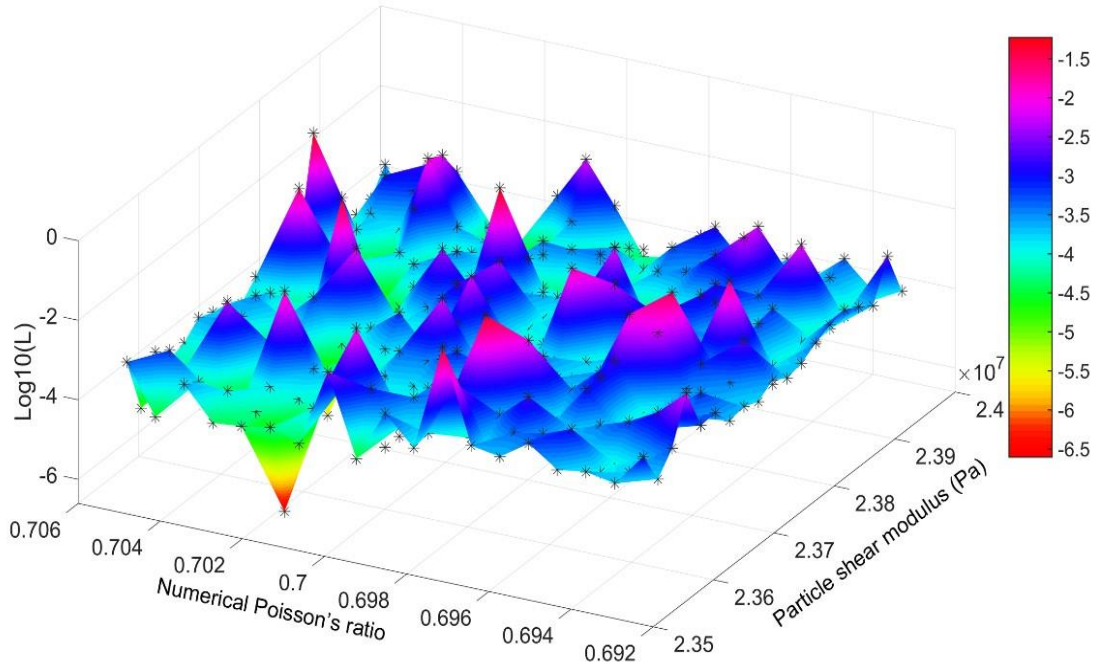

Fig. 14 A fitted surface of the logarithmic cost function against Hertz-Mindilin contact parameters in a narrow parameter space for a 3D monodisperse packing

Figures

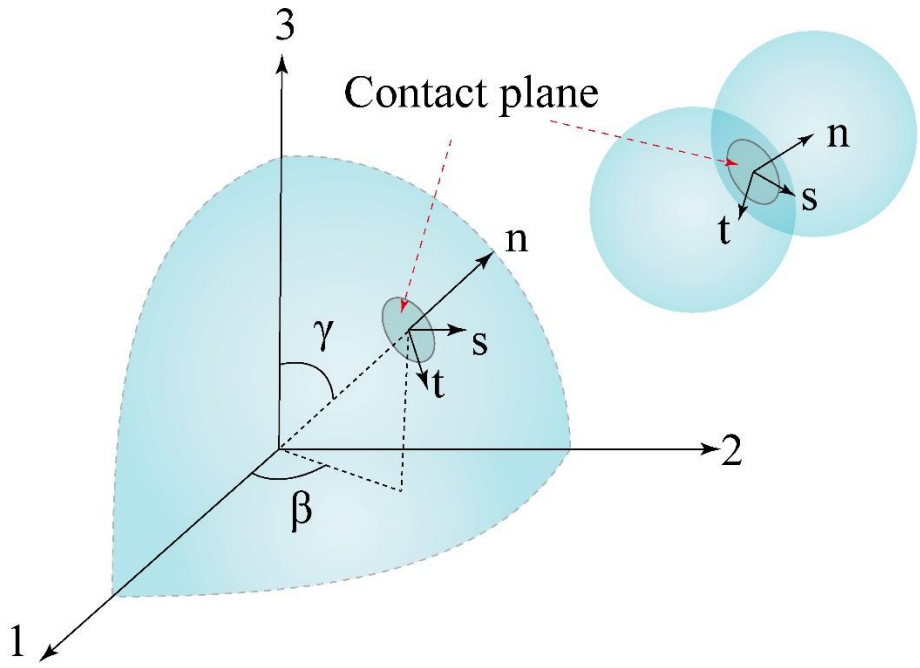

Fig.1 Spherical coordinate system and local system at c^{th} contact plane

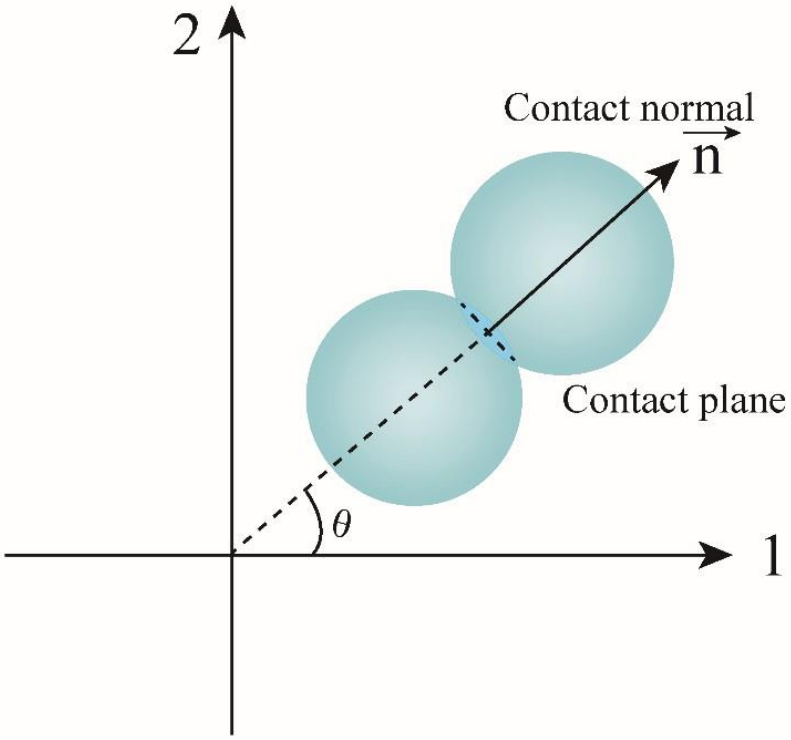

Fig. 2 Polar coordinate (2D) for directional distribution of inter-particle contact

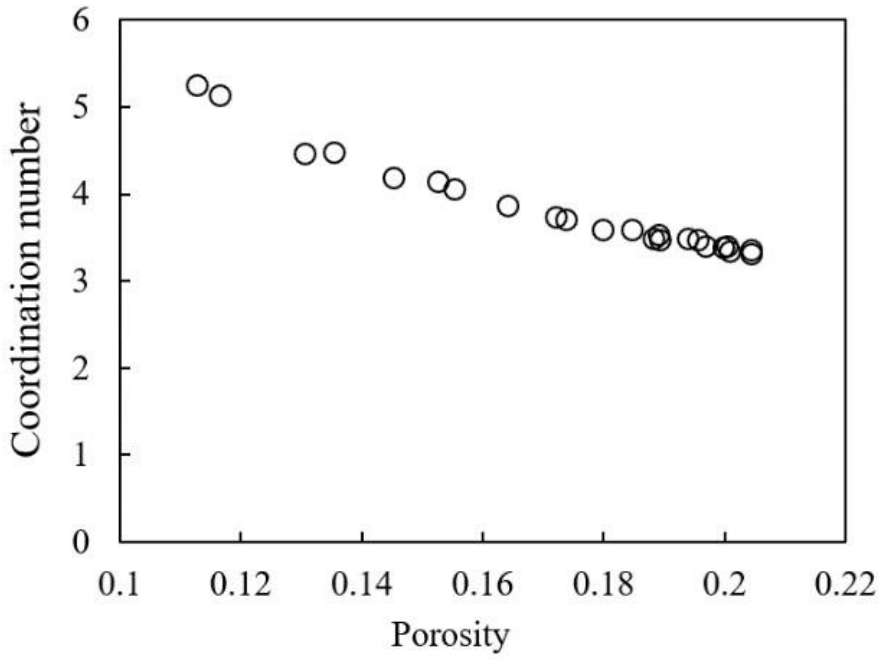

(a) 2D model

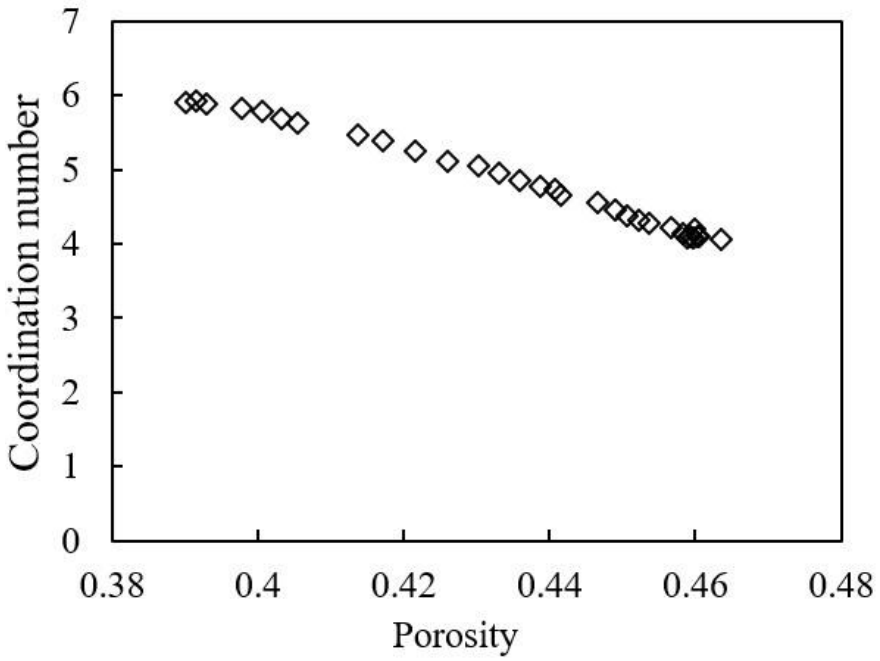

(b) 3D model

Fig.3 Porosity vs coordination number in used DEM packings (2D and 3D)

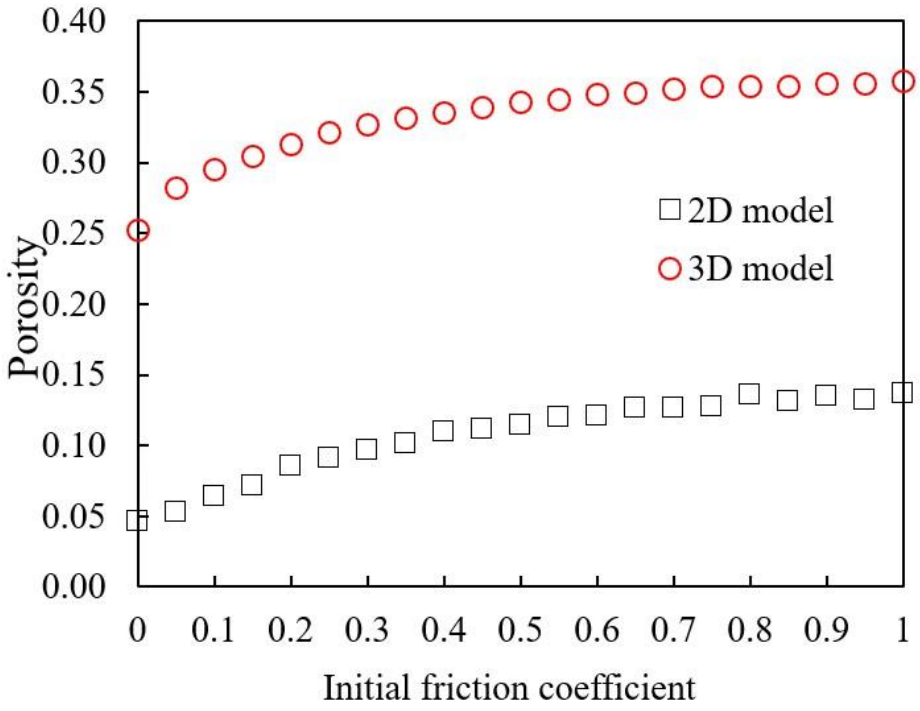

Fig.4 Initial coefficient of friction vs porosity in DEM packings

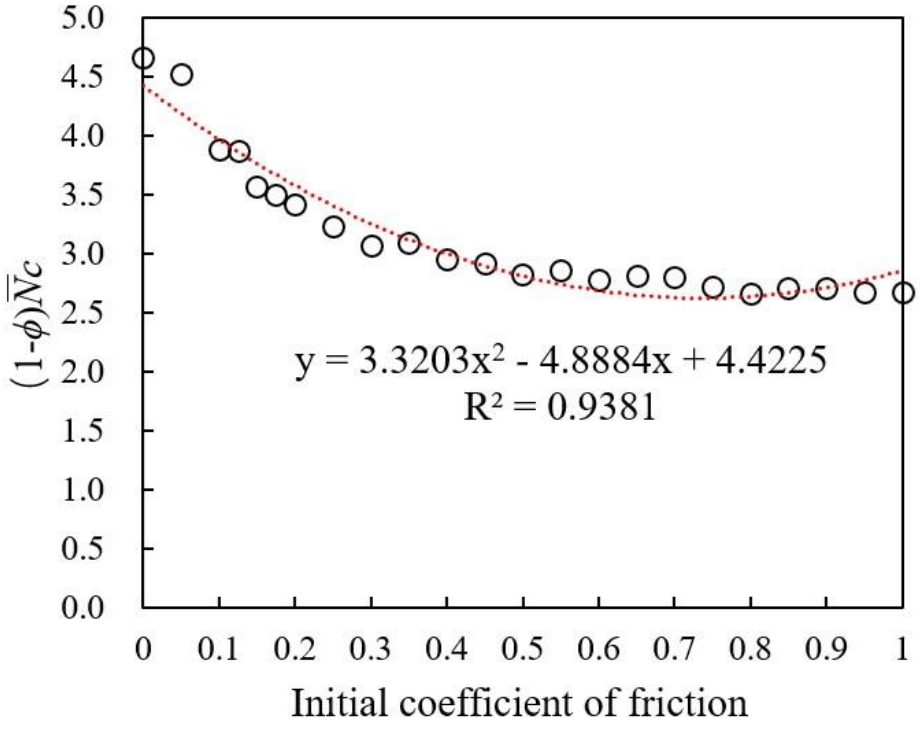

(a) 2D model

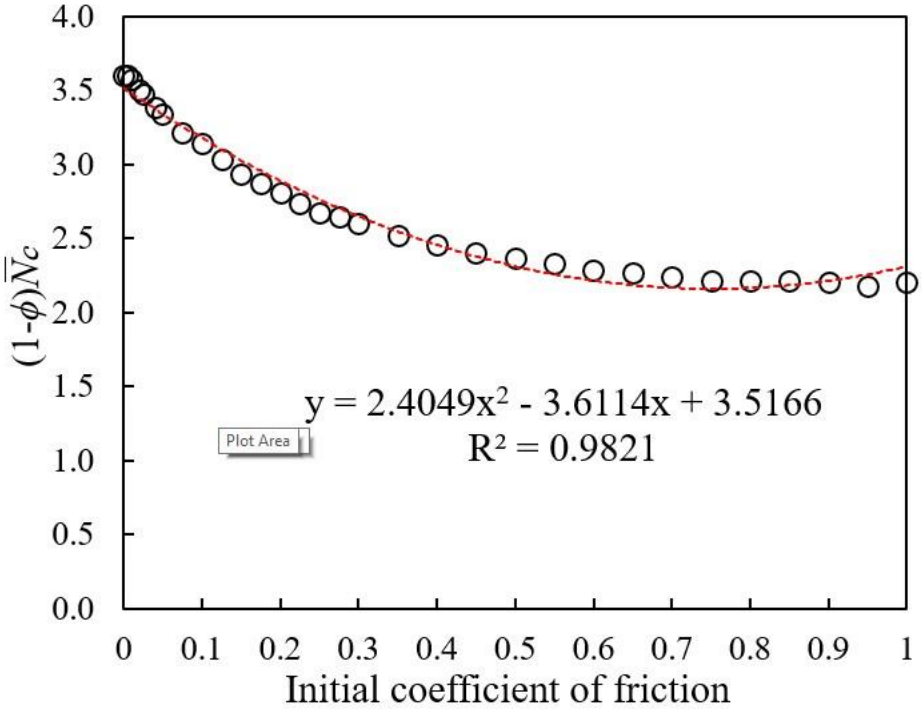

(b) 3D model

Fig. 5 Empirical relationship between initial coefficient of friction

and packing parameter $(1-)\varphi N_c$

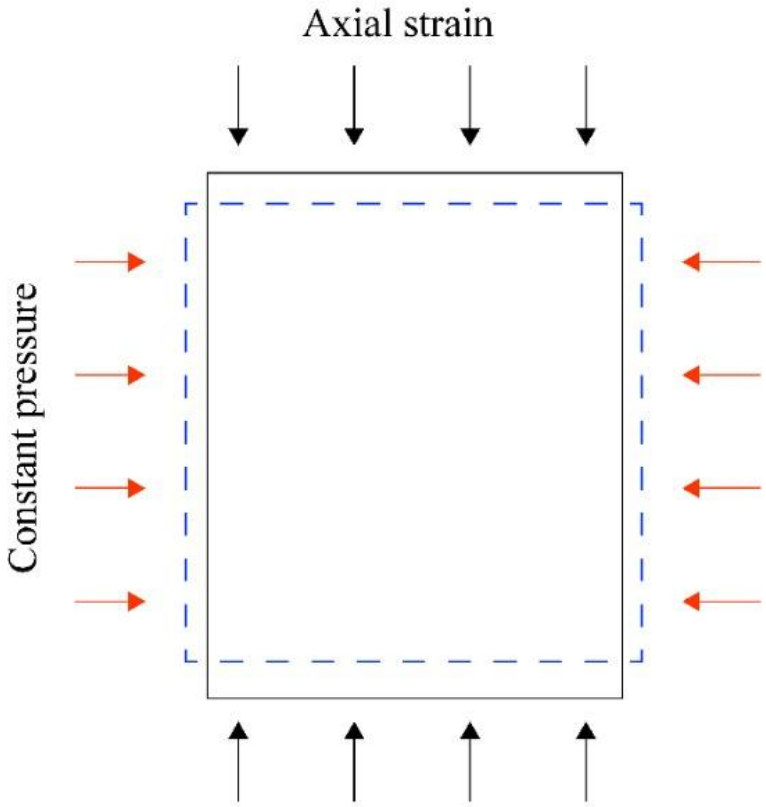

Fig.6 Schematic diagram for biaxial tests (2D and 3D)

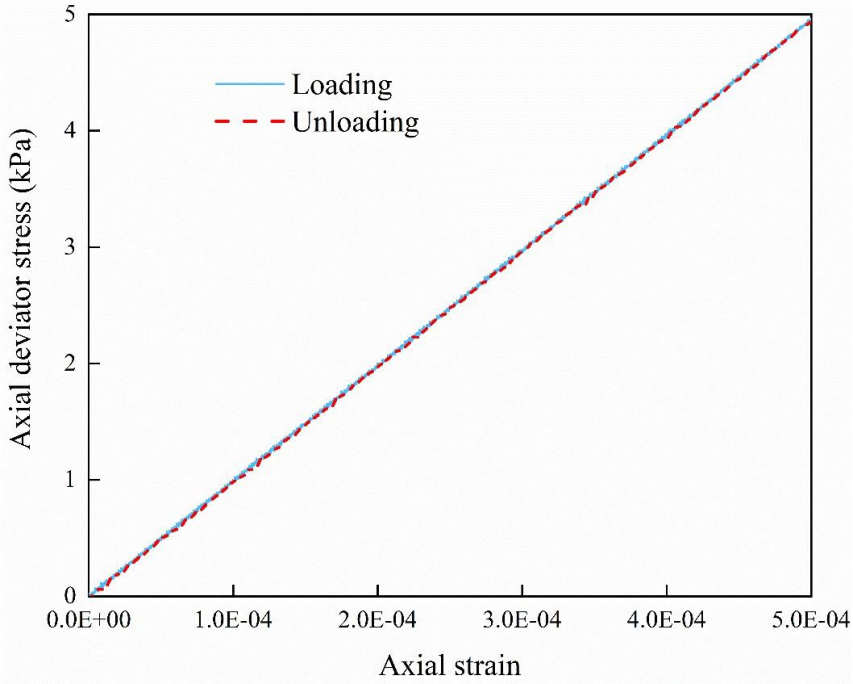

Fig.7 Axial deviatoric stress with respect to axial strain for load/unload tests

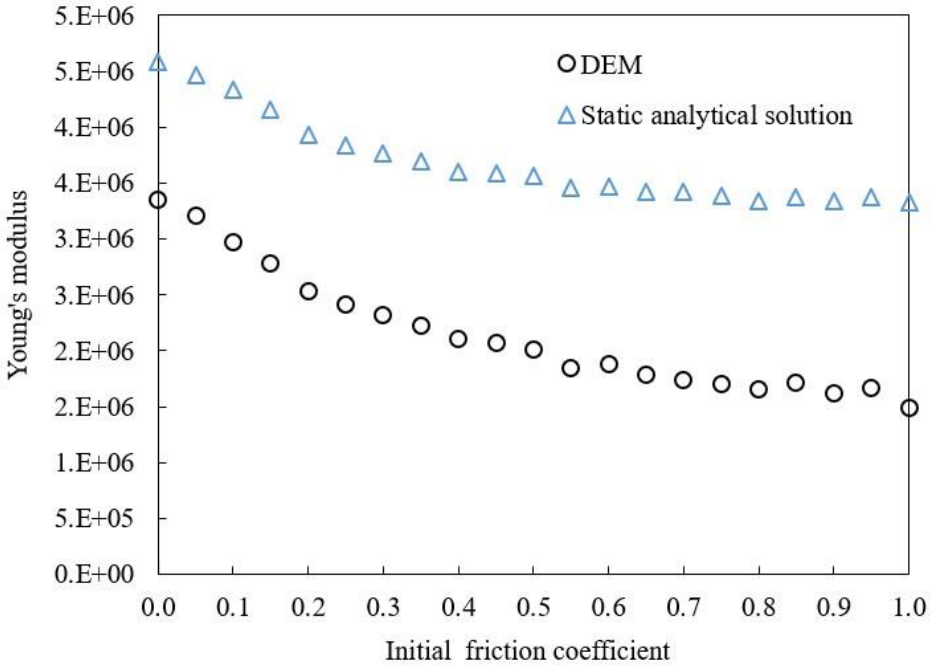

(a) 2D model

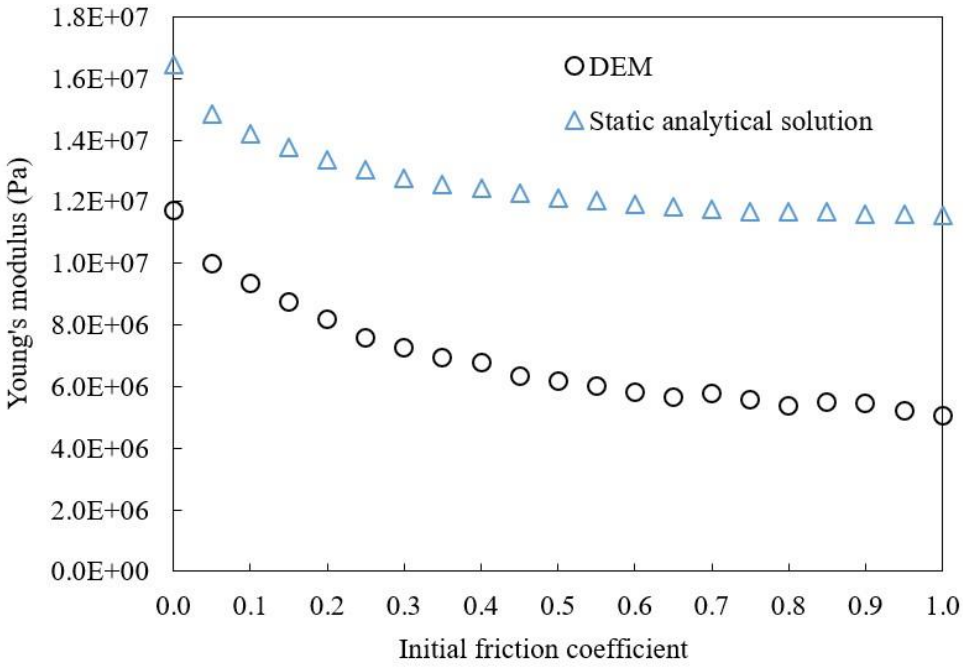

(b) 3D model

Fig.8 Comparision of macroscopic Young's modulus obtained by direct DEM simulations and static analytical solutions for different initial coefficients of friction

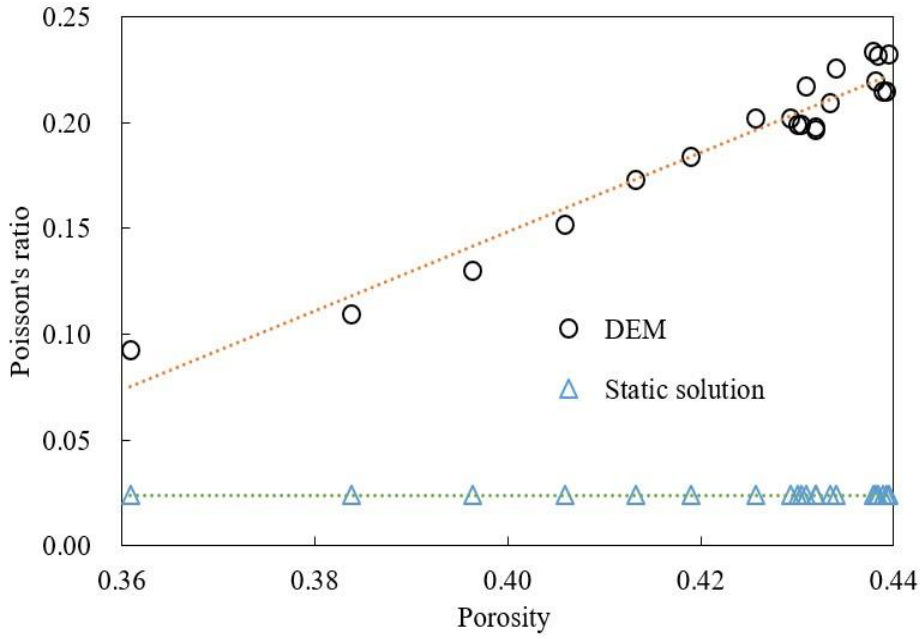

Fig.9 Comparision of macroscopic Possion's ratio obtained by direct DEM simulations and static analytical solutions for different porosities

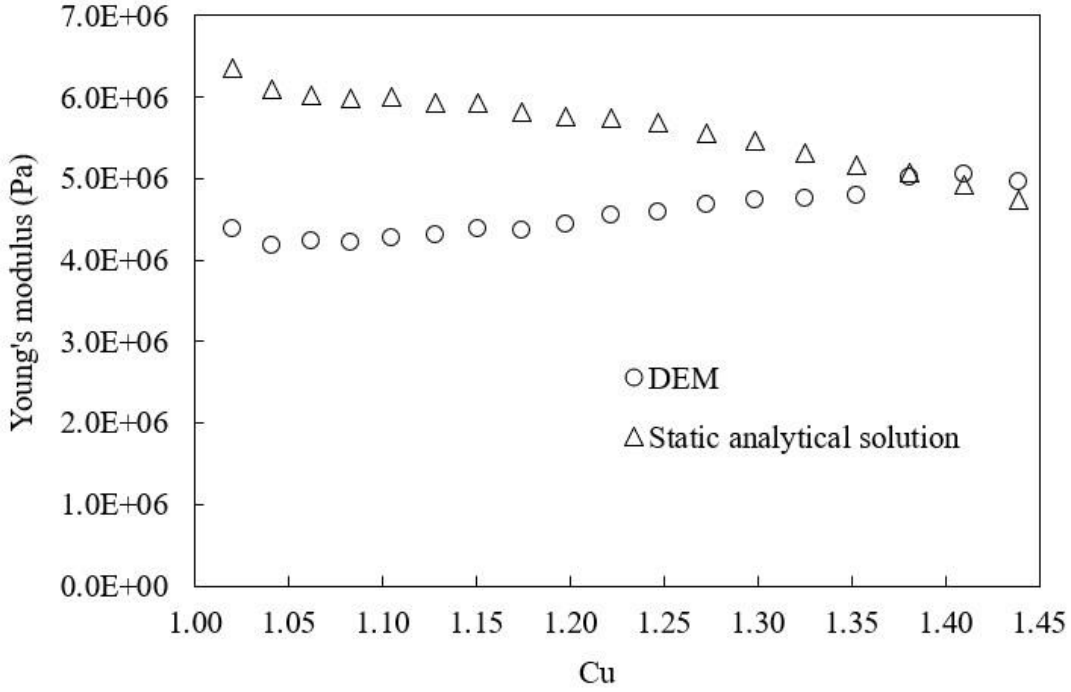

(a) 2D model

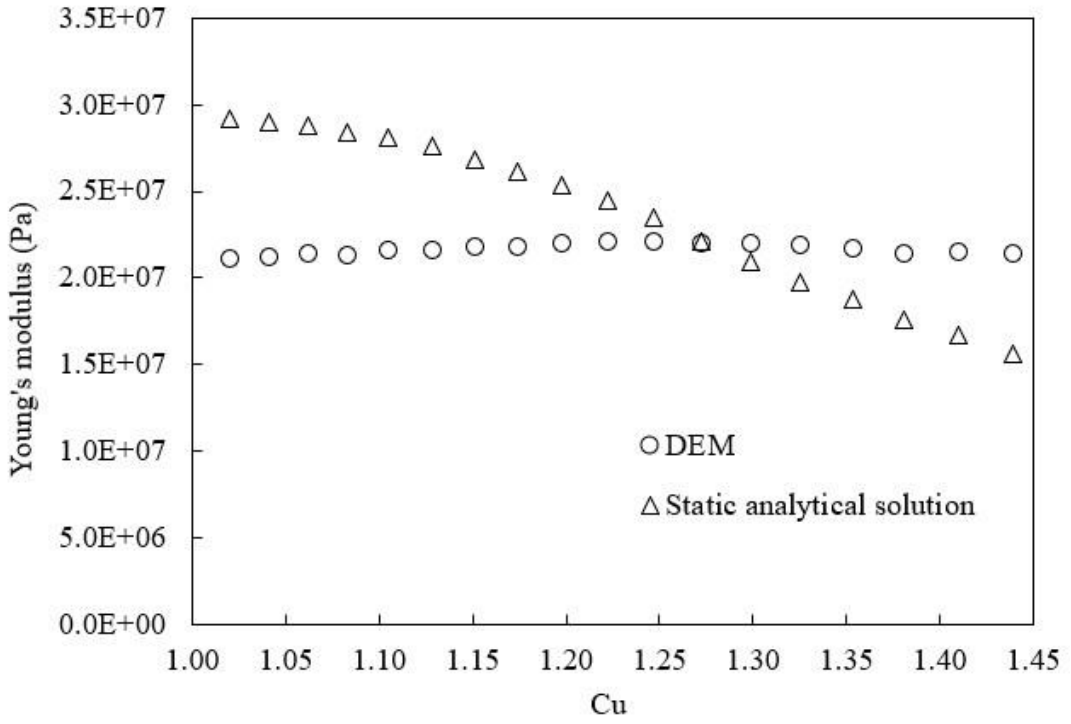

(b) 3D model

Fig.10 Macroscopic Young's modulus with respect to the coefficient of uniformity in granular packing (DEM simulations and static analytical solutions)

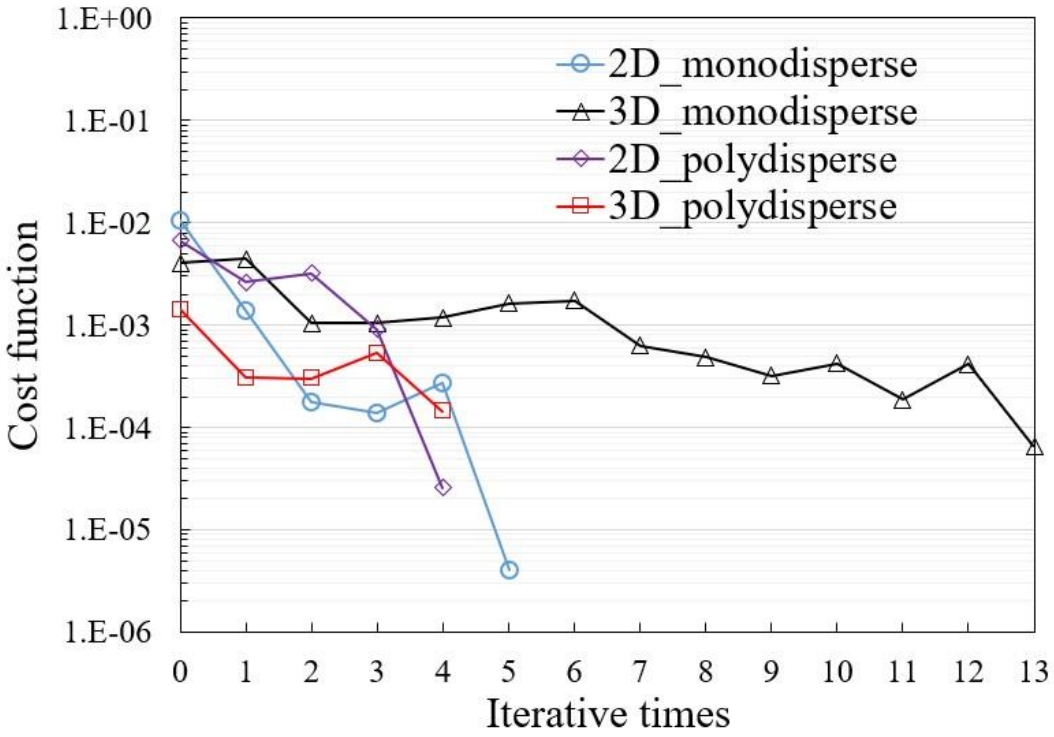

Fig.11 The convergent histories of the cost function for four test cases

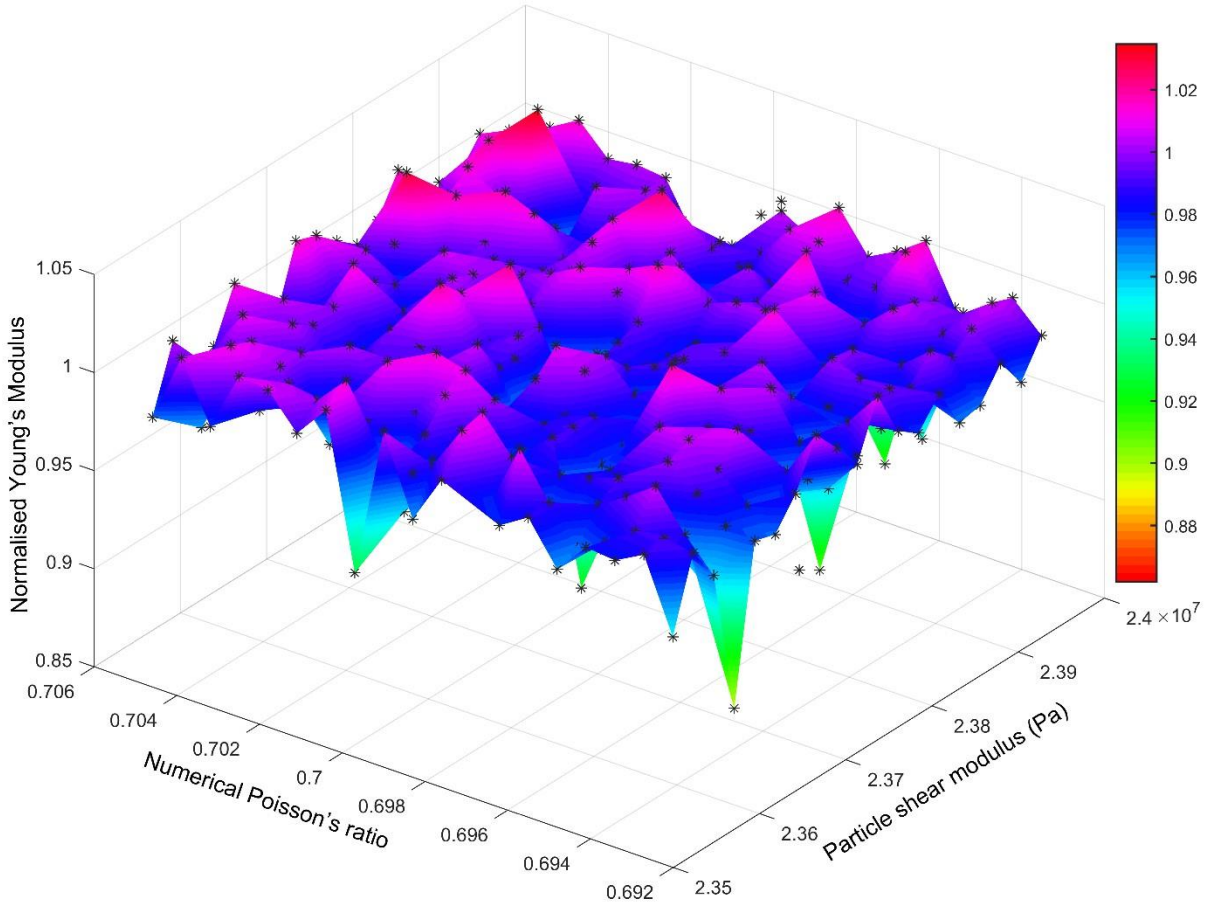

Fig. 12 A fitted surface of the normalised Young's modulus against Hertz-Mindilin contact parameters in a narrow parameter space for a 3D monodisperse packing

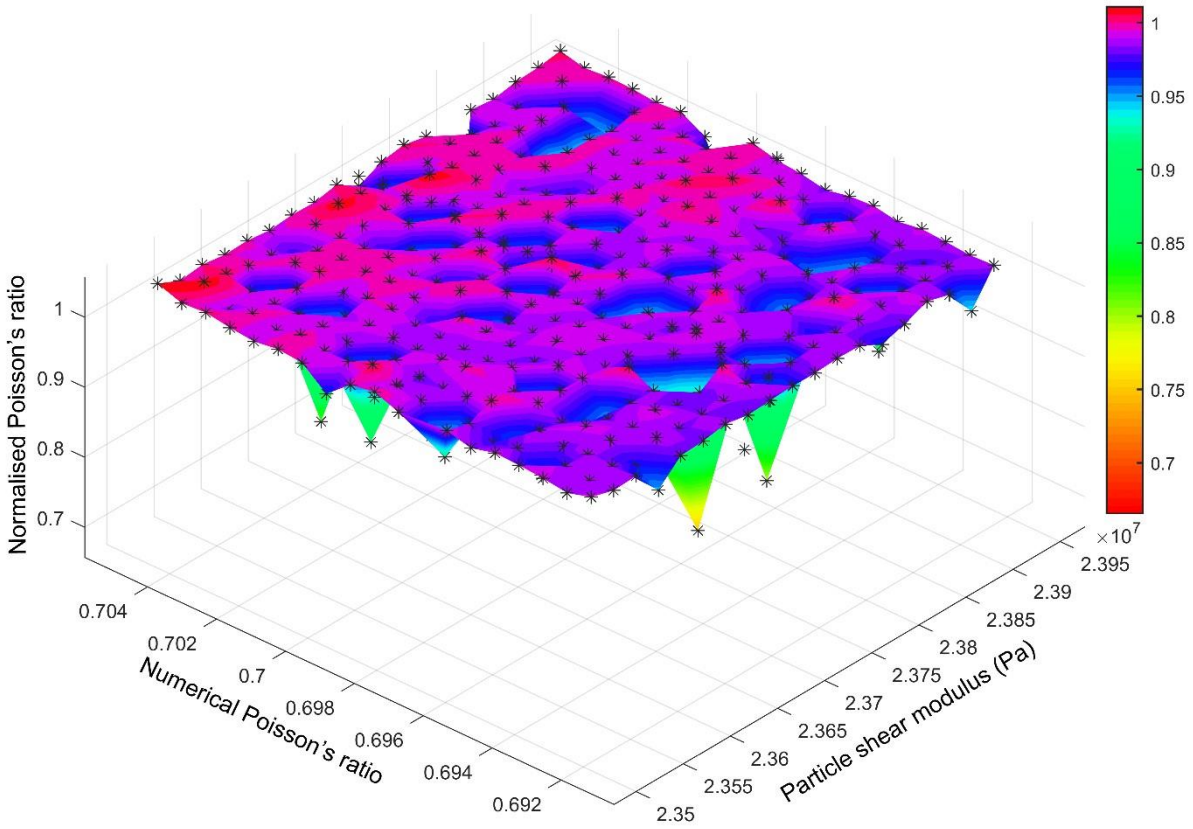

Fig. 13 A fitted surface of the normalised Poisson's ratio against Hertz-Mindilin contact parameters in a narrow parameter space for a 3D monodisperse packing

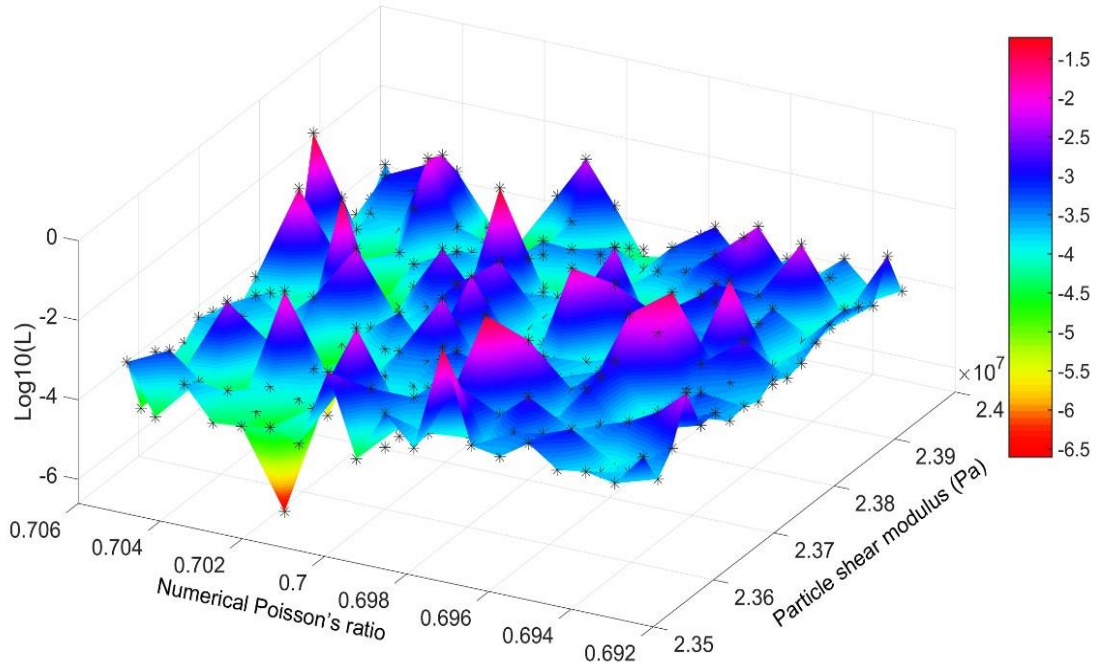

Fig. 14 A fitted surface of the logarithmic cost function against Hertz-Mindilin contact parameters in a narrow parameter space for a 3D monodisperse packing